Numerical Simulation of Electromagnetic Responses to A Seismic Source Due to the Piezoelectric Effect

Jie Zhao[1], Qianli Cheng[1], Yongxin Gao[*1], Guanqun Zhou[1], Chieh-Hung Chen[2], Xuemin Zhang[3], Yangyi-Sun[2], Simon Klemperer[4]

1. Institute of Applied Mechanics, School of Civil Engineering, Hefei University of Technology, Hefei, 230009, China

2. Institute of Geophysics and Geomatics, China University of Geosciences, Wuhan, China.

3. Institute of Earthquake Forecasting, China Earthquake Administration, Beijing 100036, China.

4. Department of Geophysics, Stanford University, Stanford, California, USA

Corresponding authors: Yongxin Gao, yongxin_gao@foxmail.com

Keypoints

- A method is presented to simulate the seismo-electromagnetic fields due to the piezoelectric effect in a 3D horizontally layered model.
- Numerical experiments are conducted to investigate the characteristics of the earthquake-induced electromagnetic fields.
- Numerical results show that the piezoelectric effect is an efficient mechanism to produce observable electromagnetic signals.

Abstract

Earthquakes are frequently accompanied by electromagnetic (EM) anomalies. These anomalies are thought to be caused by earthquakes but the generation mechanism is still unclear. The piezoelectric effect has been proposed as a possible mechanism but the EM responses to earthquakes due to such an effect has not been well understood. In this article, we study the EM signals generated by an earthquake source due to the piezoelectric effect. We develop a semi-analytical method to solve the seismic and EM fields in a 3D layered model and conduct numerical simulations to investigate the characteristics of the EM fields. The results show that the earthquake can generate two kinds of EM signals. One is the early-EM signal which arrives earlier than the seismic wave. The other is the co-seismic EM signal accompanying the seismic wave. For an $M_{\mathrm{w}} = 6.1$ earthquake the co-seismic electric field can reach ~10 μV/m and the magnetic field can reach ~10^{-4} nT. We also study the sensitivity of the co-seismic EM fields to the rock conductivity. The results show that the co-seismic EM fields are mainly affected by the conductivity of the shallow layer, and they are also affected by the conductivity of the deep layer when the top layer is thin.

Plain Language Summary

A large number of observations have shown that earthquakes can produce the electromagnetic (EM) disturbance. Many theories have been proposed to explain the EM anomaly, and the piezoelectric effect is one of the plausible mechanisms. Under stress, the positive and negative charge centers of quartz crystals are shifted, resulting in the polarization, which is manifested macroscopically as the EM radiation from quartz-rich rocks induced by earthquakes, i.e., the piezoelectric effect of earthquakes. In this paper, an analytically-based method is presented to simulate the earthquake-induced EM disturbances due to the piezoelectric effect. The simulation results show that earthquakes can produce two kinds of EM signals. One is the early-EM wave signal which travels much faster than the seismic wave and the other is the co-seismic EM signal that appears simultaneously with the seismic wave. Based on the sensitivity analysis of the EM signal we find that the EM signal is sensitive to the conductivity of shallow rocks, and the conductivity of deep rocks can also affect the EM signal. The results show that the EM fields produced by the piezoelectric effect during an earthquake are detectable.

Keywords: Earthquake; Piezoelectric Effect; Electromagnetic Anomalies; Numerical Simulations.

1. Introduction

Earthquake can produce temporal and spatial variations of electromagnetic (EM) anomalies. People have noticed this phenomenon for a long time and recorded a large number of observation data (Abdul Azeez et al., 2009; Gao et al., 2016, 2019; Gershenzon et al., 1993; Iyemori et al., 1996; Johnston & Mueller, 1987; Karakelian et al., 2002; Tang et al., 2010; etc.). These records show that EM disturbances could be observed before, during and after the earthquake (Honkura et al., 2000; Okubo et al., 2011; Rikitake, 1968). Researchers proposed several mechanisms to explain this phenomenon, for example, the electrokinetic effect (Fitterman, 1979; Gao & Hu, 2010; Ishido & Mizutani, 1981; Pride, 1994), the motional induction effect (Gao et al., 2014, 2019; Gershenzon et al., 1993; Iyemori et al., 1996; Matsushima et al., 2002; Zhao et al., 2021), the piezoelectric effect (Bishop, 1981a, b; Ghomshei et al., 1988; Huang, 2002; Ogawa & Utada, 2000a, b) and the piezomagnetic effect (Sasai, 1991; Stacey, 1964; Stuart et al., 1995; Yamazaki, 2011; Zlotnicki & Cornet, 1986), etc.

Among them, the piezoelectric (PZ) effect had been nominated to account for earthquake lightning decades ago (Finkelstain et al., 1973). As is well-known, quartz crystals are widely distributed in crustal rocks. When rocks are deformed by stress, quartz crystals will become electrically polarized as the centers of positive and negative charges of the lattice shift from a micro perspective. Literatures provide that pure quartz crystals can produce ~10^{-12} C polarization charges under 1 N axial force (Bishop, 1981a, b). For the quartz-bearing rocks in earth's crust, however, the crystallographic axes of quartz ordinarily don't align in the same direction, hence different crystals' polarized

charges probably cancel each other and this would critically reduce the overall polarization. Tuck et al. (1977) suggested that the crystallographic axes orientations of quartz in rocks are arbitrary so that the polarization due to stress would neutralize, which means that the piezoelectric effect of quartz-bearing rocks is only a statistical effect. He doubted the presence of the real piezoelectric fabric in rocks. Bishop (1981a, b) experimentally measured the piezoelectric coefficient of mylonite and compared it with the result calculated from the quartz aggregates, which confirmed the presence of the piezoelectric fabric. He also pointed out that the piezoelectric coefficient of the quartz-bearing rocks is about one-thousandth of that of a pure quartz according to the measurements of other rocks. Similar to the single crystal, the symmetry groups can be used to characterize quartz aggregates as well, such as '∞m', '∞2', '6m2' or other symmetries. Ghomshei et al. (1988) and Ghomshei & Templeton (1989) also demonstrated the presence of the piezoelectric fabric of *a*-axis in quartz-bearing rocks through piezoelectric coefficient measurements in different directions of coarse-grained quartz vein specimens as well as through neutron diffraction analysis.

Numerous researchers have carried out experiments and theoretical studies on the seismo-electromagnetic (SEM) phenomena arising from the PZ effect and achieved remarkable progress. EM signals experimentally measured during rupture, stick-slip and other tests of quartz-bearing rocks can explain the SEM phenomena to some extends. Nitsan (1977) found that the rupture of quartz-bearing rocks can generate radio frequency EM transients, and the frequency of the EM radiation tend to increase as the size of rock grains decreases. Ogawa et al. (1985) recorded the broadband electric signal

released from granite when it was struck or fractured and estimated it using PZE. His results indicated that the PZ effect might be the generation mechanism of the released electric signal. Yoshida et al. (1997) and Takeuchi & Nagahama (2006) conducted stick-slip experiments on granite and pegmatite respectively. They both detected the EM signal from rock samples and implied that it might be caused by the PZE. Sasaoka et al. (1998) and Wei et al. (2020) also believed that the PZ effect might be a reason for the EM signal generated from the quartz-bearing rock while it is stressed or fractured after their electrical measurements on granite and other rocks. Yoshida & Ogawa (2004) and Yavorovich et al. (2016) measured and analyzed the EM responses from different rocks under acoustic emission stimulations. They hold the view that PZE plays a critical role in the EM radiation phenomenon of quartz-bearing rocks. Furthermore, Russel et al. (1992) conducted a field electrical measurement on a quartz vein using hammering. He obtained the SEM signal from the quartz vein interface and suggested that it is likely to be generated by the PZ effect. These above studies demonstrated that quartz-rich rocks could release EM signals as being fractured or stressed, and suggested that the PZ effect could be responsible for it.

Other scholars theoretically explored the generation mechanism of rocks electrification and SEM phenomena and achieved quite a few results. Takeuchi & Nagahama (2002) estimated the surface charge of the quartzite and claimed that it is possible the hole and electron trapping centers due to frictional slipping rather than the PZ effect lead to the SEM phenomena. Gernets et al. (2004) studied the components of the polarization currents that caused by the fracturing of quartz-bearing rocks under

mechanical stress, and analyzed the amplitude-frequency characteristics of the EM emission. As for earthquake EM phenomena, Sornette & Sornette (1990) pointed out that the PZ effect can be a likely explanation for the telluric wave activity before the earthquake. Ikeya et al. (1997) maintained that the earthquake lightning and SEM anomalies might be attributed to the electric pulses generated by stress before and during the earthquake after they estimated the charges density considering the PZ effect in the fault. In addition, Huang (2002) proposed a fault model to explain co-seismic EM disturbances based on the PZ effect and the elastic dislocation theory and applied it to the interpretation of the EM disturbances of a real earthquake. Wang (2021) estimated the minimum stress that can generate EM signals before the earthquake using the 1D piezoelectric fault model. Ogawa & Utada, (2000a) simulated the electric field produced by the incidence of a tele-seismic wave into an underground piezoelectric body in frequency domain and discussed its features. Besides, he simulated the EM wave directly generated from the slip of a point dislocation in a homogeneous full-space in time domain based on the PZ effect and drawn the conclusion that the direct EM signal is weak (Ogawa & Utada, 2000b).

The above works suggest that the PZ effect in crustal rocks is a possible and effective mechanism for the generation of SEM anomalies. However, there still lacks sufficient understanding of the SEM field arising from such an effect. For instance, Ogawa's results were obtained in a full-space model which does not contain any interface (Ogawa & Utada, 2000a, b). The real crust usually contains interfaces which include the free surface and interfaces between different rocks. It is necessary to study

the characteristics of the EM field produced by the earthquake in the stratum with interfaces resulting from the PZ effect.

Considering the existence of the free surface and underground interfaces, we study the EM response relating to the earthquake source induced by the PZ effect in a horizontally layered model in this paper. We propose a semi-analytical method for calculating the SEM field and conduct numerical experiments to investigate the properties of the SEM anomalies due to the PZ effect.

The rest part of the article is arranged as follows. In section 2, we present the governing equations in the frequency domain, introduce the surface harmonic coordinates to obtain two sets of decoupled equations and solve them using the global matrix method. In section 3, we conduct numerical simulations to investigate the characteristics of the EM signals generated by seismic sources due to the piezoelectric effect. Finally, in sections 4 and 5, we give the discussion and conclusions.

2. Theoretical Formulations

In this paper, we assume that piezoelectric fabric of *a*-axis exists in crustal rocks. When earthquake occurs, a macroscopic polarization will be generated in quartz-bearing rocks due to the PZ effect which can generate the SEM signals subsequently. The full coupled SEM equations resulting from the piezoelectricity in the frequency domain are presented at first in this section. Then we derive two sets of decoupled equations using the Fourier transform and the surface harmonic vector expansion in a horizontal layered model. Solutions of the equations in the frequency-wavenumber domain are obtained

using the global matrix method afterwards. Finally, the results in the time-space domain are achieved by applying the inverse Fourier transform and the Hankel transform.

2.1. Governing Equations

In an isotropic homogeneous elastic and piezoelectric medium, the seismic and EM waves satisfy the following coupling equations in the frequency domain.

$$\nabla \cdot \boldsymbol{\tau} + \mathbf{F} = -\omega^2 \rho \mathbf{u}, \tag{1}$$

$$\boldsymbol{\tau} = \lambda(\nabla \cdot \mathbf{u})\boldsymbol{I} + G(\nabla \mathbf{u} + \mathbf{u}\nabla), \tag{2}$$

$$\nabla \times \mathbf{E} = i\omega\mu\mathbf{H}, \tag{3}$$

$$\nabla \times \mathbf{H} = -i\omega\left(\tilde{\varepsilon}\mathbf{E} + \mathbf{p}\right) + \mathbf{J}_s, \tag{4}$$

$$\mathbf{B} = \mu\mathbf{H}, \tag{5}$$

$$\mathbf{p} = \boldsymbol{d}\boldsymbol{\tau}', \tag{6}$$

in which $\boldsymbol{\tau}$ is the stress, $\mathbf{F}$ is the body force, ω is the angular frequency, ρ is the density of the medium, $\mathbf{u}$ is the displacement. λ and G are lamé constants, and $\boldsymbol{I}$ is the unit matrix. $\mathbf{E}$ and $\mathbf{H}$ denote the electric and magnetic fields respectively, $\mathbf{B}$ is the magnetic flux density, $\tilde{\varepsilon}$ and μ are the equivalent dielectric permittivity and the magnetic permeability of the medium. $\boldsymbol{\tau}'$ is the Voigt vector of stress tensor, which can be expressed in cylindrical coordinates as

$$\boldsymbol{\tau}' = \left(\tau_{rr} \quad \tau_{\theta\theta} \quad \tau_{zz} \quad \tau_{\theta z} \quad \tau_{rz} \quad \tau_{r\theta}\right)^{\mathrm{T}}. \tag{7}$$

And $\boldsymbol{d}$ is the piezoelectric modulus, $\mathbf{p}$ is the polarization vector, $\mathbf{J}_s$ is the external current source and i is the imaginary unit.

It should be noted that the expression of $\boldsymbol{d}$ depends on the symmetry of the quartz aggregate. It is supposed in this paper that the symmetry of the quartz aggregate in the Earth's crust is $'\infty m'$. That is to say the quartz aggregate consists of equal parts of two enantiomorphs (left hand and right hand), and the crystallographic axes of which are anti-parallel to each other (Bishop, 1981a, b). In this case the piezoelectric modulus $\boldsymbol{d}$ can be expressed as

$$\boldsymbol{d}=\begin{pmatrix} 0 & 0 & 0 & 0 & -2d_0 & 0 \\ 0 & 0 & 0 & -2d_0 & 0 & 0 \\ -d_0 & -d_0 & 2d_0 & 0 & 0 & 0 \end{pmatrix}, \tag{8}$$

where $d_0 = 5\times10^{-16}$ C / N, which is about one thousandth of the pure quartz's modulus.

Eq.(6) manifests the coupling between seismic and EM waves, indicating that the stress generated by seismic waves can induce the electric polarization. It should be noted that the seismic-induced EM fields can also stimulate the secondary stress through the inverse piezoelectric effect. However, the piezoelectric coefficient adopted in this paper is considerably small (~10^{-15} C/N) so that the secondary stress is tiny relative to the primary field. Therefore, in this paper, the EM to seismic feedback is neglected and only the seismic to EM conversion is considered.

2.2. Derivation of the Surface Harmonic Expansions

A set of complete and orthogonal surface harmonic vectors are introduced,

$$\begin{cases} \mathbf{S}_k^m(r,\theta) = -iJ_m'(kr)e^{im\theta}\mathbf{e}_r + \dfrac{m}{kr}J_m(kr)e^{im\theta}\mathbf{e}_\theta \\ \mathbf{T}_k^m(r,\theta) = \dfrac{m}{kr}J_m(kr)e^{im\theta}\mathbf{e}_r + iJ_m'(kr)e^{im\theta}\mathbf{e}_\theta \\ \mathbf{R}_k^m(r,\theta) = J_m(kr)e^{im\theta}\mathbf{e}_z \end{cases}. \tag{9}$$

$J_m(kr)$ is the Bessel function of order *m*, where *m* depends on the symmetry of the source. It could be 0, ±1 or ±2 for the seismic moment tensor source. $\mathbf{e}_r$, $\mathbf{e}_\theta$, $\mathbf{e}_z$ are the basis vectors of the cylindrical coordinates. $\mathbf{S}_k^m$, $\mathbf{T}_k^m$, $\mathbf{R}_k^m$ constitute a set of complete orthogonal coordinates, referred to as surface harmonic coordinate basis. In addition, *k* denotes the wavenumber.

A vector $\boldsymbol{\xi}(r,\theta,z)$ in cylindrical coordinates can be expanded using the surface harmonic vectors as below

$$\boldsymbol{\xi}(r,\theta,z)=\frac{1}{2\pi}\sum_{m=-\infty}^{+\infty}\int_0^{+\infty}\left[\xi_{S,m}(z,k)\mathbf{S}_k^m(r,\theta)+\xi_{T,m}(z,k)\mathbf{T}_k^m(r,\theta)+\xi_{R,m}(z,k)\mathbf{R}_k^m(r,\theta)\right]k\mathrm{d}k \quad . \tag{10}$$

$\xi_{S,m}(z,k)$, $\xi_{T,m}(z,k)$ and $\xi_{R,m}(z,k)$ are the surface harmonic components of the vector $\boldsymbol{\xi}$, which can be yielded through the following integrals

$$\begin{cases}\xi_{S,m}(z,k)=\int_0^{2\pi}\int_0^{+\infty}\boldsymbol{\xi}(r,\theta,z)\cdot\left[\mathbf{S}_k^m(r,\theta)\right]^* r\mathrm{d}r\mathrm{d}\theta\\ \xi_{T,m}(z,k)=\int_0^{2\pi}\int_0^{+\infty}\boldsymbol{\xi}(r,\theta,z)\cdot\left[\mathbf{T}_k^m(r,\theta)\right]^* r\mathrm{d}r\mathrm{d}\theta\\ \xi_{R,m}(z,k)=\int_0^{2\pi}\int_0^{+\infty}\boldsymbol{\xi}(r,\theta,z)\cdot\left[\mathbf{R}_k^m(r,\theta)\right]^* r\mathrm{d}r\mathrm{d}\theta\end{cases}, \tag{11}$$

where $[\ ]^*$ denotes conjugating.

Conversely, if the surface harmonic components of $\boldsymbol{\xi}$ are given, their cylindrical components can be obtained as well, i.e.,

$$\begin{cases} \xi_r(r,\theta,z)=\dfrac{1}{2\pi}\displaystyle\sum_{m=-\infty}^{+\infty}\int_0^{+\infty}\left[\xi_{T,m}(z,k)\frac{m}{kr}J_m(kr)e^{im\theta}-\xi_{S,m}(z,k)iJ'_m(kr)e^{im\theta}\right]k\mathrm{d}k \\ \xi_\theta(r,\theta,z)=\dfrac{1}{2\pi}\displaystyle\sum_{m=-\infty}^{+\infty}\int_0^{+\infty}\left[\xi_{T,m}(z,k)iJ'_m(kr)e^{im\theta}+\xi_{S,m}(z,k)\frac{m}{kr}J_m(kr)e^{im\theta}\right]k\mathrm{d}k \\ \xi_z(r,\theta,z)=\dfrac{1}{2\pi}\displaystyle\sum_{m=-\infty}^{+\infty}\int_0^{+\infty}\left[\xi_{R,m}(z,k)J_m(kr)e^{im\theta}\right]k\mathrm{d}k \end{cases}.$$

(12)

Let $\mathbf{Q}$ denote the stress vector in the horizontal plane. Separately applying eq.(10) on the displacement $\mathbf{u}(r,\theta,z)$, body force $\mathbf{F}(r,\theta,z)$, stress $\mathbf{Q}(r,\theta,z)$, electric field $\mathbf{E}(r,\theta,z)$ and magnetic field $\mathbf{H}(r,\theta,z)$, we obtain

$$\mathbf{u}(r,\theta,z)=\frac{1}{2\pi}\sum_{m=-\infty}^{+\infty}\int_0^{+\infty}\left[u_{S,m}(z,k)\mathbf{S}_k^m(r,\theta)+u_{T,m}(z,k)\mathbf{T}_k^m(r,\theta)+u_{R,m}(z,k)\mathbf{R}_k^m(r,\theta)\right]k\mathrm{d}k \quad ,$$

(13)

$$\mathbf{F}(r,\theta,z)=\frac{1}{2\pi}\sum_{m=-\infty}^{+\infty}\int_0^{+\infty}\left[F_{S,m}(z,k)\mathbf{S}_k^m(r,\theta)+F_{T,m}(z,k)\mathbf{T}_k^m(r,\theta)+F_{R,m}(z,k)\mathbf{R}_k^m(r,\theta)\right]k\mathrm{d}k \quad ,$$

(14)

$$\mathbf{Q}(r,\theta,z)=\frac{1}{2\pi}\sum_{m=-\infty}^{+\infty}\int_0^{+\infty}\left[Q_{S,m}(z,k)\mathbf{S}_k^m(r,\theta)+Q_{T,m}(z,k)\mathbf{T}_k^m(r,\theta)+Q_{R,m}(z,k)\mathbf{R}_k^m(r,\theta)\right]k\mathrm{d}k \quad ,$$

(15)

$$\mathbf{E}(r,\theta,z)=\frac{1}{2\pi}\sum_{m=-\infty}^{+\infty}\int_0^{+\infty}\left[E_{S,m}(z,k)\mathbf{S}_k^m(r,\theta)+E_{T,m}(z,k)\mathbf{T}_k^m(r,\theta)+E_{R,m}(z,k)\mathbf{R}_k^m(r,\theta)\right]k\mathrm{d}k \quad ,$$

(16)

and

$$\mathbf{H}(r,\theta,z)=\frac{1}{2\pi}\sum_{m=-\infty}^{+\infty}\int_0^{+\infty}\left[H_{S,m}(z,k)\mathbf{S}_k^m(r,\theta)+H_{T,m}(z,k)\mathbf{T}_k^m(r,\theta)+H_{R,m}(z,k)\mathbf{R}_k^m(r,\theta)\right]k\mathrm{d}k \quad .$$

(17)

Employing eqs (6)-(8) we yield the cylindrical components of the electric polarization vector **p**, i.e.,

$$\begin{cases} p_r = -2d_0\tau_{rz} \\ p_\theta = -2d_0\tau_{\theta z} \\ p_z = -d_0\tau_{rr} - d_0\tau_{\theta\theta} + 2d_0\tau_{zz} \end{cases} . \tag{18}$$

Further applying eqs (2), (13) and (15) we successively obtain the expressions of **p** in the surface harmonic coordinates system,

$$p_r = -2d_0 \cdot \frac{1}{2\pi} \sum_{m=-\infty}^{+\infty} \int_0^{+\infty} \left[Q_{T,m}(z,k) \frac{m}{kr} J_m(kr) e^{im\theta} - Q_{S,m}(z,k) i J_m'(kr) e^{im\theta} \right] k\mathrm{d}k , \tag{19}$$

$$p_\theta = -2d_0 \cdot \frac{1}{2\pi} \sum_{m=-\infty}^{+\infty} \int_0^{+\infty} \left[Q_{T,m}(z,k) i J_m'(kr) e^{im\theta} + Q_{S,m}(z,k) \frac{m}{kr} J_m(kr) e^{im\theta} \right] k\mathrm{d}k \tag{20}$$

and

$$p_z = \frac{1}{2\pi} \sum_{m=-\infty}^{+\infty} \int_0^{+\infty} \left[2d_0 Q_{R,m}(z,k) - 2d_0(\lambda+G) iku_{S,m}(z,k) - 2d_0\lambda \frac{\partial u_{R,m}}{\partial z}(z,k) \right] J_m(kr) e^{im\theta} k\mathrm{d}k$$

. (21)

Two independent sets of equations could be derived by substituting the surface harmonic expansions of the displacement, body force, stress, electric field, magnetic field and the electric polarization into the governing equations (1)-(4):

$$\frac{\partial}{\partial z} \begin{pmatrix} u_S \\ u_R \\ Q_S \\ Q_R \\ E_S \\ H_T \end{pmatrix} = \begin{pmatrix} 0 & -ik & \frac{1}{G} & 0 & 0 & 0 \\ -\frac{\lambda ik}{\lambda+2G} & 0 & 0 & \frac{1}{\lambda+2G} & 0 & 0 \\ \frac{4k^2G(\lambda+G)}{\lambda+2G} - \omega^2\rho & 0 & 0 & -\frac{\lambda ik}{\lambda+2G} & 0 & 0 \\ 0 & -\omega^2\rho & -ik & 0 & 0 & 0 \\ -\frac{2d_0k^2(3\lambda G+2G^2)}{\tilde{\varepsilon}(\lambda+2G)} & 0 & 0 & -\frac{4d_0ikG}{\tilde{\varepsilon}(\lambda+2G)} & 0 & \frac{\omega^2\mu\tilde{\varepsilon}-k^2}{i\omega\tilde{\varepsilon}} \\ 0 & 0 & 2d_0i\omega & 0 & -i\omega\tilde{\varepsilon} & 0 \end{pmatrix} \begin{pmatrix} u_S \\ u_R \\ Q_S \\ Q_R \\ E_S \\ H_T \end{pmatrix} + \begin{pmatrix} 0 \\ 0 \\ -F_S \\ -F_R \\ \frac{k}{\omega\tilde{\varepsilon}} \tilde{J}_R \\ \tilde{J}_S \end{pmatrix},$$

(22)

and

$$\frac{\partial}{\partial z}\begin{pmatrix} u_T \\ Q_T \\ E_T \\ H_S \end{pmatrix} = \begin{pmatrix} 0 & \dfrac{1}{G} & 0 & 0 \\ Gk^2-\omega^2\rho & 0 & 0 & 0 \\ 0 & 0 & 0 & i\omega\mu \\ 0 & -2d_0 i\omega & \dfrac{k^2-\omega^2\mu\tilde{\varepsilon}}{i\omega\mu} & 0 \end{pmatrix}\begin{pmatrix} u_T \\ Q_T \\ E_T \\ H_S \end{pmatrix} + \begin{pmatrix} 0 \\ -F_T \\ 0 \\ -\tilde{J}_T \end{pmatrix}. \tag{23}$$

Eq.(22) only contains u_S, u_R, Q_S, Q_R, E_S and H_T, which couples the PSV and TM waves, hereafter is thus referred to as PSVTM mode equation. Eq.(23) only contains u_T, Q_T, E_T and H_S, which couples the SH and TE waves, hereafter is referred to as SHTE mode equation.

These two sets of equations can be written uniformly as shown below

$$\frac{\partial}{\partial z}\mathbf{b} = \boldsymbol{A}\mathbf{b} + \mathbf{F}, \tag{24}$$

where $\boldsymbol{A}$ is the system matrix, $\mathbf{b}$ is the displacement-stress-EM vector and $\mathbf{F}$ is the source vector.

Hence, for the PSVTM mode, we have

$$\mathbf{b}_V = \left[u_S、\ u_R、\ \tau_{SR}、\ \tau_{RR}、\ E_S、\ H_T\right]^{\mathrm{T}}, \tag{25}$$

$$\mathbf{F}_V = \left(0, 0, -F_S, -F_R, \frac{k}{\omega\tilde{\varepsilon}}\tilde{J}_R, \tilde{J}_S\right)^T, \tag{26}$$

$$\boldsymbol{A}_V = \begin{pmatrix} 0 & -ik & \frac{1}{G} & 0 & 0 & 0 \\ -\frac{\lambda ik}{\lambda+2G} & 0 & 0 & \frac{1}{\lambda+2G} & 0 & 0 \\ \frac{4k^2G(\lambda+G)}{\lambda+2G}-\omega^2\rho & 0 & 0 & -\frac{\lambda ik}{\lambda+2G} & 0 & 0 \\ 0 & -\omega^2\rho & -ik & 0 & 0 & 0 \\ -\frac{2d_0k^2(3\lambda G+2G^2)}{\tilde{\varepsilon}(\lambda+2G)} & 0 & 0 & -\frac{4d_0ikG}{\tilde{\varepsilon}(\lambda+2G)} & 0 & \frac{\omega^2\mu\tilde{\varepsilon}-k^2}{i\omega\tilde{\varepsilon}} \\ 0 & 0 & 2d_0i\omega & 0 & -i\omega\tilde{\varepsilon} & 0 \end{pmatrix}. \tag{27}$$

For the SHTE mode,

$$\mathbf{b}_T = \left[u_T、\ \tau_{TR}、\ E_T、\ H_S\right]^{\mathrm{T}}, \tag{28}$$

$$\mathbf{F}_T = \left(0, -F_T, 0, -\tilde{J}_T\right)^T, \tag{29}$$

$$\boldsymbol{A}_T = \begin{pmatrix} 0 & \frac{1}{G} & 0 & 0 \\ Gk^2-\omega^2\rho & 0 & 0 & 0 \\ 0 & 0 & 0 & i\omega\mu \\ 0 & -2d_0i\omega & \frac{k^2-\omega^2\mu\tilde{\varepsilon}}{i\omega\mu} & 0 \end{pmatrix}. \tag{30}$$

2.3. Method and Solutions

Fig 1 shows the 3D horizontal layered model. We assume that *x*-, *y*- and *z*-axis represent northward, eastward and downward directions, respectively. The zero point (0, 0, 0) is located on the earth surface. The source is located at (0, 0, *h*), where *h* denotes the source depth. Each layer is composed of the isotropic homogeneous elastic and piezoelectric medium. The seismic and EM wavefields generated by a point source in a stratified model can be solved using the Global Matrix method (Chen, 1999; Kennett & Kerry, 1979).

Eq.(24) can be written in the following form if the body force **F** is omitted

$$\frac{\partial}{\partial z}\mathbf{b}(z) = \boldsymbol{A}\mathbf{b}(z)\,. \tag{31}$$

Here we apply the eigenvalue decomposition operation on the system matrix $\boldsymbol{A}$ for the n-th layer medium

$$\boldsymbol{A}_n\boldsymbol{D}_n = \boldsymbol{D}_n\boldsymbol{\Lambda}_n\,, \tag{32}$$

where $\boldsymbol{\Lambda}_n$ and $\boldsymbol{D}_n$ are respectively the diagonal matrix of eigenvalues and the matrix of eigenvectors associated with the system matrix $\boldsymbol{A}_n$. In addition, $\boldsymbol{D}_n$ can be written in the following forms for the PSVTM and SHTE modes,

$$\boldsymbol{D}_n^{PSVTM} = \left[\mathbf{d}_n^{+P},\ \mathbf{d}_n^{-P},\ \mathbf{d}_n^{+SV},\ \mathbf{d}_n^{-SV},\ \mathbf{d}_n^{+TM},\ \mathbf{d}_n^{-TM}\right], \tag{33}$$

$$\boldsymbol{D}_n^{SHTE} = \left[\mathbf{d}_n^{+SH},\ \mathbf{d}_n^{-SH},\ \mathbf{d}_n^{+TE},\ \mathbf{d}_n^{-TE}\right]. \tag{34}$$

$\mathbf{d}_n^{+P}$, $\mathbf{d}_n^{+SV}$, $\mathbf{d}_n^{+SH}$, $\mathbf{d}_n^{+TM}$ and $\mathbf{d}_n^{+TE}$ denote the eigenvectors of down-going P, SV, SH, TM and TE waves; whereas $\mathbf{d}_n^{-P}$, $\mathbf{d}_n^{-SV}$, $\mathbf{d}_n^{-SH}$, $\mathbf{d}_n^{-TM}$ and $\mathbf{d}_n^{-TE}$ represent the eigenvectors of up-going waves. These eigenvectors represent the fundamental solutions of the displacement-stress-EM responses generated by the down- and up-going waves. Their analytical expressions are derived in Appendix A using the plane wave theory. It should be noted that $\boldsymbol{\Lambda}_n$ and $\boldsymbol{D}_n$ can also numerically solved by the eigenvalue decomposition of $\boldsymbol{A}_n$, nevertheless the precision and efficiency can be improved by adopting the analytic eigenvalues and eigenvectors.

$\boldsymbol{\Lambda}_n$ can be respectively expressed in the PSVTM and SHTE modes as

$$\boldsymbol{\Lambda}_n^{PSVTM} = diag\left(i\gamma_n^P, i\gamma_n^S, i\gamma_n^{EM}, -i\gamma_n^P, -i\gamma_n^S, -i\gamma_n^{EM}\right), \tag{35}$$

$$\boldsymbol{\Lambda}_n^{SHTE} = diag\left(i\gamma_n^S, i\gamma_n^{EM}, -i\gamma_n^S, -i\gamma_n^{EM}\right), \tag{36}$$

where γ_n^P, γ_n^S and γ_n^{EM} represent the vertical wavenumbers of the P, S and EM waves in the *n*-th layer

$$\gamma_n^j = \sqrt{\left(\omega s^j\right)^2 - k_x^2},\ j = P, S, EM\ , \tag{37}$$

in which γ_n^j has two roots and we take the root with a positive imaginary part. k_x is the horizontal wavenumber. s^j is the slowness of the P, S or EM wave, which can be determined by the following expressions

$$s_n^P = \sqrt{\frac{\rho_n}{\lambda_n + 2G_n}}\ , \tag{38}$$

$$s_n^S = \sqrt{\frac{\rho_n}{G_n}}\ , \tag{39}$$

$$s_n^{EM} = \sqrt{\mu\tilde{\varepsilon}_n}\ . \tag{40}$$

ρ_n, λ_n and G_n as well as $\tilde{\varepsilon}_n$ denote the density, lame's parameters and the equivalent dielectric permittivity of the medium in the *n*-th layer.

The liner transformation of the displacement-stress-EM vector $\mathbf{b}_n(z)$ is introduced here

$$\mathbf{b}_n(z) = \boldsymbol{D}_n(z)\mathbf{W}_n(z)\,, \tag{41}$$

where $\mathbf{W}_n(z)$ denotes the amplitude vector of seismic and EM waves at depth of *z* in the *n*-th layer. Substituting eqs (32) and (41) into eq.(31), we obtain

$$\frac{\partial}{\partial z}\mathbf{W}_n(z) = \boldsymbol{\Lambda}_n\mathbf{W}_n(z)\,. \tag{42}$$

Since $\boldsymbol{\Lambda}_n$ is a diagonal matrix, it is easy to solve $\mathbf{W}_n(z)$ from eq.(42), which can be expressed as

$$\mathbf{W}_n(z) = \boldsymbol{\Theta}\tilde{\mathbf{w}}_n\,. \tag{43}$$

$\boldsymbol{\Theta}$ is the propagation matrix of seismic and EM waves, which can be written for the PSVTM and SHTE modes respectively as

$$\boldsymbol{\Theta}^{PSVTM} = diag\left[e^{i\gamma_n^P(z-z_{n-1})}, e^{i\gamma_n^S(z-z_{n-1})}, e^{i\gamma_n^{EM}(z-z_{n-1})}, e^{i\gamma_n^P(z_n-z)}, e^{i\gamma_n^S(z_n-z)}, e^{i\gamma_n^{EM}(z_n-z)} \right], \quad (44)$$

$$\boldsymbol{\Theta}^{SHTE} = diag\left[e^{i\gamma_n^S(z-z_{n-1})}, e^{i\gamma_n^{EM}(z-z_{n-1})}, e^{i\gamma_n^S(z_n-z)}, e^{i\gamma_n^{EM}(z_n-z)} \right]. \quad (45)$$

$\tilde{\mathbf{w}}_n$ denotes the amplitude vector composed of the down- and up-going waves at interfaces in the *n*-th layer, which can be written in the following forms as well

$$\tilde{\mathbf{w}}_n^{PSVTM} = \left[A_n^{+P}, A_n^{+SV}, A_n^{+TM}, A_n^{-P}, A_n^{-SV}, A_n^{-TM} \right]^T, \quad (46)$$

$$\tilde{\mathbf{w}}_n^{SHTE} = \left[A_n^{+SH}, A_n^{+TE}, A_n^{-SH}, A_n^{-TE} \right]^T. \quad (47)$$

The amplitudes of different waves at any depth can be obtained according to eq.(43) as long as $\tilde{\mathbf{w}}_n$ is given. And the displacement-stress-EM vector $\mathbf{b}_n(z)$ can be calculated through eq.(41). $\tilde{\mathbf{w}}_n$ can be solved using boundary conditions and the source contribution (Gao et al., 2019; Haartsen & Pride, 1997).

For the seismic and EM waves propagating underground, the displacement, stress and EM fields should satisfy the continuity conditions at the interface ($z = z_n$) of any two adjacent layers, i.e.,

$$\mathbf{b}_n(z_n) = \mathbf{b}_{n+1}(z_n). \quad (48)$$

At the free surface, it requires both the traction is zero and the horizontal components of EM fields are continuous, namely

$$\left[\tau_{SR}, \ \tau_{RR} \right]_{n=1}^{\mathrm{T}} = \mathbf{0}, \quad (49)$$

$$\left[E_S, H_T \right]_{n=1}^{\mathrm{T}} = \left[E_S, H_T \right]_{n=0}^{\mathrm{T}}, \quad (50)$$

which are for the PSVTM mode, and

$$\left[\tau_{TR} \right]_{n=1} = \mathbf{0}, \quad (51)$$

$$\left[E_T, H_S\right]_{n=1}^{\mathrm{T}} = \left[E_T, H_S\right]_{n=0}^{\mathrm{T}}, \tag{52}$$

which are for the SHTE mode.

The contribution of the source can be determined by the assumption that there is a virtual interface at the depth of the source, at which the discontinuity of the displacement-stress-EM vector is defined as

$$\mathbf{S} = \mathbf{b}_s(z_{s+}) - \mathbf{b}_s(z_{s-}), \tag{53}$$

where **S** is the discontinuity vector. Different expressions of **S** for different sources are derived in Appendix B.

Combining the corresponding equations of boundary conditions at each interface and the source distribution we yield a linear system with respect to the unknown amplitudes ($\tilde{\mathbf{w}}_n$) of different waves of each layer. The amplitudes of seismic and EM waves at any depth in any layer can be obtained by solving this linear system. Then we would get the solutions of the displacement, stress, electric field and magnetic field in frequency-wavenumber domain according to eq.(41). Finally, the seismic and EM responses in time-space domain are obtained using the Hankel transform with respect to wavenumber *k* and applying the inverse frequency-time Fourier transform.

3. Numerical Simulations

3.1. Seismic and EM Responses Associated with Body Waves Generated by The Source

In this section, we conduct numerical simulations to investigate the characteristics of seismo-electromagnetic (SEM) wavefields due to the piezoelectric (PZ) effect. We first study the EM responses associated with the body waves. To do this, we adopt a full-space model to omit the influences of the free surface and other interfaces. Parameters of the medium are chosen as Rock A in Table 1. Three kinds of point sources are investigated: an explosive source that only stimulate PSVTM mode waves, a center of rotation source that only stimulate SHTE mode waves and a double-couple source that can stimulate both two modes. The latter is often used to simulate an earthquake fault slip. The time function of the source is the Ricker wavelet with a center frequency $f_0 = 1\,\mathrm{Hz}$ and a delay of $t_0 = 1\,\mathrm{s}$, i.e.,

$$s_0(t) = \left[1 - 2\pi^2 f_0^2 (t - t_0)^2\right] e^{-\pi^2 f_0^2 (t-t_0)^2}. \tag{54}$$

This time function is used for all the numerical simulations in this paper.

3.1.1. Seismic and EM Responses Generated by An Explosive Source

We first consider the excitation of an explosive source, which can be expressed by the seismic moment tensor as $M_{xx} = M_{yy} = M_{zz} = 1.5831 \times 10^{18}$ Nm with other moment tensor components being 0. According to Appendix B, the discontinuity vectors of the PSVTM and SHTE modes have the following forms

$$\mathbf{S}^{PSVTM}=\left[0,\frac{1}{\lambda+2G}M_{zz},\frac{ik}{2}\left(M_{xx}+M_{yy}-\frac{2\lambda}{\lambda+2G}M_{zz}\right),0,-\frac{4d_0ikG}{\tilde{\varepsilon}\left(\lambda+2G\right)}M_{zz},0\right]^{\mathrm{T}},\quad(55)$$

$$\mathbf{S}^{SHTE}=\left[0,\ 0,\ 0,\ 0\right]^{\mathrm{T}}.\quad(56)$$

Consequently, only the PSVTM mode waves are produced by the explosive source. The source and receiver are shown in Fig 2(a). The source is located at the origin and hence the coordinates of the receiver can be determined as (50 km, 70 km, -10 km). The displacement, electric and magnetic fields recorded at the observation point are presented in Fig 3.

In the records of the displacement the direct P wave can be seen, which arrives at about $t=13.5\,\mathrm{s}$, that is consistent with the theoretical arrival time $88.3\,\mathrm{km}/6.5\,\mathrm{km\cdot s^{-1}}=13.58\,\mathrm{s}$. We can find two signals in the electric and magnetic records. The first one arrives at the same time of the P wave. It is the co-seismic electric (or magnetic) field induced by the P wave. The amplitude of the displacement field at the receiver is ~10^{-3} m, and the amplitude of the electric field is ~1 μV/m, which is detectable. The magnetic field is ~10^{-3} nT which is weak but still could be detected by current EM monitoring equipment. The other one appears at about t = 0 s. It is the direct EM wave excited by the explosive source. Because the EM wave propagates much faster than the seismic wave, it almost instantaneously arrives at the receiver after the source launches. However, the direct EM signal is much smaller than the co-seismic signal, thus it is amplified by a factor of 10^5 to be apparent in Fig 3.

It is worth noting that the vertical component of the co-seismic magnetic field is 0 for both the direct EM wave and the co-seismic signal accompanying the P wave. This suggests that the P wave cannot generate vertical magnetic fields. Moreover, the direct

EM wave has no response in the vertical magnetic field indicating that the EM wave generated by the explosive source is the TM wave.

We further study the spatial distribution features of the direct EM wave. As shown in Fig 2(b), 10201 receivers are located on the horizontal plane that is perpendicular to the *z*-axis and 20 km above the source. These receivers constitute a rectangular receiver array within a region of $-50\ \text{km} < x < 50\ \text{km}$, $-50\ \text{km} < y < 50\ \text{km}$. We calculate the direct EM wave at each receiver and draw the amplitude distribution of each component of the electric and magnetic fields in Fig 4.

We can see that the direct EM signal is strongest near the center of the receiver array (i.e., the epicenter), where the electric field is ~0.0015 μV/m and the magnetic field is ~10^{-5} nT. The EM signal becomes weak as the receiver gets far away from the epicenter. The amplitudes of the horizontal components are azimuth dependent. In addition, we also find that electric and magnetic fields are symmetric about coordinates. E_x and B_y are symmetric about *y*-axis but with inverse polarizations, E_y and B_x are symmetric about *x*-axis with inverse polarizations similarly.

3.1.2. Seismic and EM Responses Generated by A Center of Rotation Source

In this section we consider a source with the seismic moment tensor $M_{xy} = -M_{yx} = 1.5831 \times 10^{18}$ Nm (other moment tensor components are set to be 0). According to Appendix B, the corresponding discontinuity vectors are

$$\mathbf{S}^{SHTE} = \left[0, \frac{ik}{2} M_{xy} - \frac{ik}{2} M_{yx}, 0, 0 \right]^{\mathrm{T}}, \tag{57}$$

$$\mathbf{S}^{PSVTM} = \mathbf{0}, \tag{58}$$

which indicate that the source can only generate the SHTE mode waves.

The displacement, electric and magnetic wavefields at the receiver (50 km, 70 km, -10 km) are presented in Fig 5. The seismic signal arriving at about t = 22.6 s is the SH wave generated by the source. Because the SH wave does not produce the vertical displacement, U_z is zero. Two EM signals can be found in the electric and magnetic records. The first one arriving at t = 0 s is the EM wave directly excited by the source, and the other arriving at t = 22.6 s is the co-seismic wave inducing by the SH wave. The electric fields reach ~0.01 μV/m and the magnetic fields are ~10^{-4} nT when the displacement fields are ~0.01 m. Comparing Figs. 3 and 4, we see that the displacements produced by the P and S waves are on the same order while the co-seismic electric and magnetic fields produced by the S wave are 1~2 orders weaker than those produced by the P wave, indicating that the S wave has weaker capability in producing the co-seismic EM fields than the P wave. In addition, there is no record in the vertical component of electric fields, indicating that the SH wave does not generate the vertical electric field. The direct EM wave does not produce the vertical electric field, implying that it is the TE wave.

We also calculate the direct EM wave at the receivers on the rectangular region 20 km above the x-y plane and present their spatial distribution in Fig 6. It can be seen that the EM wave is stronger when the receiver is closer to the epicenter. The transverse components of EM fields are azimuth dependent as well. They also have a certain

symmetry: E_x and B_y are symmetric about x-axis with inverted polarizations; E_y and B_x are symmetric about y-axis with inverted polarizations likewise.

3.1.3. Seismic and EM Responses Generated by A Fault Slip Source

In this section, we simulate the seismic and EM responses to a fault slip source. Consider an $M_w = 6.1$ earthquake with strike 90°, dip 90°, slip 90° and depth 10 km. The corresponding moment tensor components are $M_{xz} = M_{zx} = 1.5831 \times 10^{18}$ Nm (other components are set to be 0). The displacement, electric and magnetic wavefields at the receiver (50 km, 70 km, -10 km) are presented in Fig 7.

We can see the P and S waves in the displacement records. In the EM records, we can see the co-seismic electric and magnetic fields associated with the P and S waves. The EM fields associated with the P wave are smaller than those associated with the S wave. The displacement of the S wave is ~10^{-3} m, and the corresponding co-seismic electric field reaches ~10 μV/m, showing that the PZ effect has sufficient conversion efficiency to produce observable electric signal. The co-seismic magnetic field of the S wave is merely ~10^{-3} nT, which is also within the detectability of the current magnetic sensors. In addition, the co-seismic magnetic field of the P wave is smaller than that of the S wave. The EM signal arriving at $t = 0$ s is the EM wave directly generated by the source, indicating that EM wave can be excited by the fault slip due to the PZ effect but it's amplitude is much smaller than that of the co-seismic EM signal (note that the electric and magnetic fields of the direct EM wave are all magnified in Fig 7).

The EM wave generated by the source is very important for earthquake early warning because it arrives much earlier than the seismic waves. As we did in section 3.1.1 and 3.1.2, we also calculate the direct EM wave in the array on the horizontal plane, and investigate the radiation pattern of the EM wave (Figure 8). As we can see, the closer the receiver is to the epicenter, the stronger the EM signal will be. The electric field in the vicinity of the epicenter can reach about 0.03 μV/m and the magnetic field can reach about 10^{-4} nT, which are both within the detectability of the current EM equipment. Furthermore, each component of the electric and magnetic fields exhibits azimuth dependence, especially E_y and B_x, which show obvious four-quadrant distribution patterns.

3.2. Seismic and EM Responses in the Stratified Models

In section 3.1, the EM responses associated with body waves (including the body seismic waves and body EM wave) excited by the earthquake source in a uniform full space are studied. In this section we study the seismic and EM responses due to the PZ effect in the stratified models.

3.2.1. Numerical Simulations of Seismic and EM Fields in A Half-space Model

We first consider a half-space model as shown in Fig 2(c). Parameters of the medium are chosen according to Rock 3 shown in Table 1. We adopt the same fault slip source as in section 3.1.3, i.e., $M_{xz} = M_{zx} = 1.5831 \times 10^{18}$ Nm . The depth of the source

is 10 km, and the source time function is the Ricker wavelet with the central frequency of 1 Hz and delay of 1 s.

The waveforms of three components (radial, tangential and vertical) of the displacement, electric and magnetic fields at the receiver (50 km, 70 km, 0.1 m) are presented in Fig 9. There are the P, S waves and the Rayleigh (R) wave in the displacement records. The co-seismic electric signals associated these three waves can be identified in all three components of the electric fields (Figs 9d-9f). The horizontal co-seismic electric fields associated with the P wave are amplified by a factor of 20 in Fig 9 to make it to be apparent. Moreover, we can see the R wave in Fig 9(e) clearly, indicating that the contribution of PSV mode waves cannot be ignored in E_t.

Figs 9(g)-9(i) show the co-seismic magnetic fields. The signals associated with the P, S and R waves in the tangential component B_t are amplified by 10 times. We can see obvious co-seismic magnetic signals of the S wave in all three components of magnetic fields. The co-seismic magnetic signals of P and R waves can only be seen in the tangential component. According to eq.(12), the P and R waves should also generate B_r because the PSVTM mode waves have contribution to B_r if $m \neq 0$ (the fault slip source here is not axisymmetric and hence $m \neq 0$). They are not apparent in the waveform of B_r in Fig 9(g) because they are weaker than the co-seismic magnetic field produced by the S wave. In addition, because the PSVTM waves do not generate the vertical magnetic fields, there are no P and R waves in the waveform of B_z. This suggests that B_r and B_z are mainly contributed by the SHTE mode waves whereas B_t is mainly contributed by the PSVTM mode waves.

In Figs 9(h)-9(i), we can see the early-EM signals arriving before the seismic waves in the magnetic records. There are two pulses with different arrival times. The first one arrives at ~0 s, which should be the direct EM wave generated by the source. It arrives at the observation point almost as soon as it is excited because it's high travelling speed. The arrival time of the second one is ~2.5 s, agreeing with the time for S waves travelling from the source to the free surface perpendicularly, i.e., $10\ \mathrm{km} / 2.9\ \mathrm{km \cdot s^{-1}} = 2.56\ \mathrm{s}$. Therefore, it might be the EM wave generated by S waves at the free surface. Similar phenomenon can be seen in the simulated EM signals based on the electrokinetic effect in Gao et al. (2013), who concluded that the S waves can generate reflected and critically-refracted EM waves due to the electrokinetic effect at the free surface, which arrive much earlier than the seismic waves. The early-EM waves should have the electric responses, too. Nevertheless, they are not apparent in the electric records because they are much weaker than the co-seismic electric fields associated with S waves.

The displacements of the S wave are ~0.01 m, while the corresponding co-seismic electric fields reach ~10 μV/m, which could be easily measured by the modern instrument, implying that the PZ effect has sufficient conversion efficiency to generate observable electric signals. The co-seismic magnetic fields are ~10^{-4} nT, which are relatively weak but still can be detected by precise magnetic sensors. Comparing Figs. 7 and 9, we find that the co-seismic magnetic fields (~10^{-4} nT) generated by the S wave (displacement of ~0.01 m) near the free surface are weaker than those (~10^{-3} nT) generated by the body S wave with smaller amplitudes (displacement of ~0.001 m) in

a full space, implying that the existence of the free surface has a significant negative effect on the generation of the co-seismic magnetic fields.

3.2.2. Numerical Simulations of Seismic and EM Fields in A Three-layers Model

In this section we conduct numerical experiments in a three-layers model as shown in Fig 2(d). The parameters of different layers are chosen according to Rocks 1-3 in Table 1. The source and the receiver are the same as specified in section 3.2.1.

The seismic and EM wavefields at the receiver (50 km, 70 km, 0.1 m) are showed in Fig 10. The waveforms in Fig 10 are somewhat complex compared to those in the half-space model (Fig 9) because of the multiple reflections and refractions taking place at interfaces in the three-layers model.

The maximum amplitude of the displacement field is ~0.05 m in Fig 10. The co-seismic electric field reaches ~10 μV/m, and the magnetic field reaches 10^{-3} nT. The co-seismic electric and magnetic fields associated with S waves are the strongest, which dominate the EM records. We can see the early-EM waves that travel much faster than seismic waves in the magnetic records. Its duration is longer than that of the early-EMs wave in the half-space model. This is because of the fact that the seismic waves repetitiously excite EM waves at different interfaces. The early-EM waves cannot be seen in electric records because they are much smaller than co-seismic electric fields.

From the results of the half-space model (Fig 9) and the three-layers model (Fig 10), we find that the tangential component of the co-seismic magnetic field is weaker

than both the radial and vertical components. This is a notable characteristic of the co-seismic magnetic field induced by the PZ effect, which probably could be used to distinguish from the magnetic fields induced by other mechanisms. In contrary, the radial component of the co-seismic electric field is higher than the other two components especially higher than the vertical component. Furthermore, the numerical examples based on the electrokinetic effect showed that, the vertical component of the co-seismic electric field is more than 2 orders of magnitude higher than the horizontal components (Gao, 2010; Hu & Gao, 2011). This demonstrating that the PZ effect differs with the EK effect in producing co-seismic electric fields.

3.3. Influence of Rock Conductivity on Co-seismic EM Fields

The EM anomalies generated by earthquakes depend on the focal mechanism as well as the properties of rocks, especially their conductivities. In this section, we study the influence of the conductivity on the EM responses induced by the PZ effect.

3.3.1. Influence of the Conductivity of the Layer Where the Receiver is Located

We first consider a half-space model. As shown in Fig 2(c), the fault slip source with $M_{xz} = M_{zx} = 1.5831 \times 10^{18}$ Nm is located 10 km below the Earth's surface. The time function is the Ricker wavelet with a center frequency of 1 Hz and a delay of 1 s. The receiver is located at (50 km, 70 km, 0.1 m). Parameters of the rock in the half-space are chosen according to Rock A in Table 1, except that the conductivities are

chosen as 0.01 S/m and 0.05 S/m, respectively. We compare the synthetic EM fields resulting from different rock conductivities.

The red lines in Fig 11 are the SEM responses when the conductivity is 0.01 S/m, and the blue lines are the responses when the conductivity is 0.05 S/m. The displacement fields are not showed in Fig 11 because they are not affected by the conductivity (the EM-to-seismic feedback is neglected).

We find that with the increasing conductivity, the amplitudes of co-seismic electric fields of P, S and R waves decrease, while the amplitudes of co-seismic magnetic fields almost remain unchanged, except that the early-EM wave diminishes. Note that the EM waves bear physical attenuation during their propagation, and specifically, the higher the conductivity becomes, the stronger the attenuation is. The conductivity can influence the conversion efficiency of the EM waves generated by the source as well. That is to say, the influence of the conductivity on the early-EM wave is a combined effect of the changes of seismic-to-electric conversion efficiency and physical attenuation. However, it is difficult to infer how the conductivity affects the seismic-to-electric conversion from the simulations shown in Fig11. For the co-seismic EM fields, because the conductivity does not affect the propagation of the seismic waves, changes of the co-seismic EM fields are merely due to that the seismic-to-EM conversion efficiency varies with the conductivity. Therefore, hereafter we focus on how the co-seismic EM responses change with the rock conductivity.

We calculate the co-seismic EM fields for the conductivities being 10^{-4} S/m, 10^{-3} S/m, 10^{-2} S/m, 10^{-1} S/m and 1 S/m, separately, and extract the maximum value of the co-seismic fields of P, S and R waves, respectively, and then display them in Fig 12.

As can be seen from Figs 12(a)-12(c), the co-seismic electric fields associated with P, S and R waves all decrease approximately linearly with the increase of the conductivity, and particularly E_t is smaller than both E_r and E_z. Figs 10(d)-(f) provide the amplitude variations of co-seismic magnetic fields with different conductivities. As we discussed in section 3,2.1, the magnetic fields produced by P and R waves should also have responses in B_r, thus might change with the conductivity. However, they are much smaller than the co-seismic magnetic signal produced by the S wave and hence are not apparent in B_r components (Figs 9,10,11). Therefore, only the co-seismic magnetic field of the S wave is extracted and shown in Fig 12(d). Besides, because the P and R waves do not produce vertical magnetic fields, only the co-seismic magnetic field of S wave in B_z is shown Fig 12(f).

It can be seen that the co-seismic magnetic fields change little with the conductivity. When the conductivity is less than ~0.1 S/m, the magnetic fields B_r and B_z hardly change with the conductivity, but they tend to slightly change when the conductivity is more than ~0.1 S/m. In the B_t component, the magnetic fields of P and R waves are smaller than those of the S wave. In addition, we find that B_t is two orders of magnitude smaller than B_r and B_z.

3.3.2. Influence of the Conductivity of the Deep Layer

In the previous section, we used a half-space model to study the influence of the conductivity of the layer where the receiver is located (hereafter noted as σ_1). In order to investigate whether the co-seismic EM fields will be affected by the conductivity of the deep layer (hereafter noted as σ_2) or not, a two-layers model is adopted here. The thickness of the upper layer is 100m. The elastic parameters of the two layers are the same, which are chosen according to Rock 3 in Table1. We change the conductivity of the lower layer and keep the conductivity of the upper layer as $\sigma_1 = 0.01\,\mathrm{S/m}$. The parameters of the source are the same as in section 3.3.1.

The red lines in Fig 13 represent the SEM responses when $\sigma_2 = 0.01\,\mathrm{S/m}$. In this case, the two-layers model is equivalent to a half-space model because the conductivities of the two layers are the same. The blue lines represent the SEM responses when σ_2 is increased to 0.05 S/m. It can be seen that when σ_2 increases the horizontal components of the co-seismic electric fields decrease yet the vertical component does not change. For the co-seismic magnetic fields however, the radial and vertical components are almost unchanged when σ_2 increases. As for the tangential component, the co-seismic magnetic field associated with the P wave decreases, whereas the co-seismic magnetic fields of S and R waves increase. These results are different from those in the half-space model (Fig 11).

In order to better understand the influence of the conductivity of the deep layer on the SEM fields, we calculate the EM responses when σ_2 is 10^{-4} S/m, 10^{-3} S/m, 10^{-2}

S/m, 10^{-1} S/m and 1 S/m, separately. Then we draw the maximum amplitudes of co-seismic electric and magnetic fields for different σ_2 in Fig 14.

From Fig 14 we can find that the co-seismic electric fields of P, S and R waves in E_r and E_t components all decrease as σ_2 increases. But they differ from the results in Figs 12(a)-(c), in which the co-seismic electric fields decrease approximately linearly. In addition, E_z does not vary, indicating that it is not sensitive to σ_2. The co-seismic magnetic fields B_r and B_z hardly change with σ_2, but slightly decrease only when $\sigma_2 > 0.1\,\mathrm{S/m}$, which is analogous to that in the half-space model (Fig 12). B_t is different from both B_r and B_z, showing that the magnetic fields associated with S and R waves are minimal when $\sigma_2 = 0.01\,\mathrm{S/m}$ and will increase no matter σ_2 is larger or smaller than 0.01 S/m. Besides, Fig 14(e) illustrates that the co-seismic magnetic field of the P wave decreases as σ_2 increases.

Notice that the two-layers model would become a half-space model when the conductivity of the deep layer $\sigma_2 = 0.01\,\mathrm{S/m}$ ($\sigma_2 = \sigma_1$). The co-seismic EM fields calculated under the condition $\sigma_2 = \sigma_1$ can be referred as reference signals. For the horizontal components of the co-seismic electric fields, when the conductivity of the deep layer is higher than that of the top layer where the receiver is located (i.e., $\sigma_2 > \sigma_1$), the co-seismic electric field is higher than the half-space reference signals. For $\sigma_2 < \sigma_1$, the co-seismic electric field is smaller than the reference signals. This provides a penitential method to characterize the underground deep electrical properties. Since the shallow rock conductivity can be easily measured, we can calculate the reference co-seismic signals using the half-space model specified by the shallow

conductivity. For instance, according to Figs 14(a) and 14(b), if the observed horizontal co-seismic electric field is larger than the reference signals, it can be inferred that the conductivity of deep layer is lower than that of the shallow layer. However, we cannot achieve this point using the co-seismic magnetic fields (the tangential component).

The phenomenon that the co-seismic EM responses vary with the rock conductivity probably can be explained by the evanescent wave theory. Due to the PZ effect, the seismic waves can generate EM waves at the interface of two media. Considering the depth of the source (10 km) and the epicentral distance (~86 km), the P wave is incident with an angle of about 83.4° to the interface which is 100 m below the free surface. According to Snell's law, the reflection angle of the EM wave, which travels much faster than the seismic wave, will exceed 90° and thus becomes an evanescent or inhomogeneous EM wave which propagates along the interface and attenuates rapidly away from the interface (Ren et al., 2016; Zhao et al., 2021). Such an EM wave permeates upwards and received by the receiver as a part of the total co-seismic EM responses associated with the P wave shown in Fig 13. Similarly, the co-seismic EM fields associated with the S and R waves also contain the contributions from the evanescent EM waves converted from the S and R waves.

Since the evanescent EM wave decays fast along the vertical direction, if the receiver is far from the interface, the contribution of the evanescent EM wave to the co-seismic EM fields may decrease. To confirm this assumption, we increase the thickness of the first layer to 5 km. We still keep the conductivity of the first layer (σ_1) as 0.01 S/m and change the conductivity of the second layer (σ_2).The maximal amplitudes of

the co-seismic EM fields for different values of σ_2 are calculated and shown in Fig 15. We can see that neither the electric field nor the magnetic field changes with σ_2 at this point. This is because the evanescent wave stimulated by seismic waves at the interface becomes so weak that they contribute little to the co-seismic EM field due to the high attenuation.

The above findings suggest that the EM fields associated with seismic waves due to the PZ effect depend not only on the conductivity of the upper layer of the crust but also on that of the deep layer. In general, the co-seismic electric field is more sensitive to the medium's conductivity, which tends to decrease as the conductivity increases; whereas the co-seismic magnetic field is not distinctly sensitive to the conductivity unless the conductivity is fairly high ($>0.1\,\mathrm{S/m}$). Furthermore, the dependence of the co-seismic EM fields on the rock conductivity implies a potential application of the co-seismic EM fields in characterizing the underground electric structure.

4. Discussion

The above numerical examples reveal that the earthquake can produce two kinds of EM signals owing to the PZ effect. One is the co-seismic EM signal accompanying the seismic waves; the other is the early-EM signal, including the EM wave radiated directly from the hypocenter and that converted from a seismic wave at an interface.

Studies show that the co-seismic and early- EM signals can also be generated due to the electric kinetic (EK) effect and the motional induction (MI) effect (Gao et al., 2014; Gao et al., 2019; Gao, 2010； Hu & Gao, 2011; Zhao et al., 2021). Here we

compare the EM fields produced by the PZ effect with those produced by the EK effect and the MI effect.

At first, we compare the co-seismic magnetic fields. According to Fig 3 in Gao et al., (2014), Fig 2 in Gao et al., (2019) and Fig 2 in Zhao et al., (2021), the P and SV waves can generate both horizontal and vertical magnetic fields due to the MI effect. However, according to Gao (2010) and Gao et al., (2013), the P and SV waves can only generate horizontal components of magnetic fields due to the EK effect and have no vertical magnetic response. The numerical examples presented in this paper suggest that the P wave cannot induce the vertical component of magnetic fields due to the PZ effect either (Fig 3), which can be illustrated by eq.(A48) in Appendix A. In addition, the SV wave cannot stimulate the vertical magnetic field either according to eq.(A52). The fact that PSV mode waves do not generate the vertical magnetic field is an important feature to distinguish the PZ effect from the MI effect, but it cannot be used to distinguish the PZ effect from the EK effect.

Then we discuss the sensitivity of the co-seismic EM fields to the rock conductivity. From Zhao et al., (2021) we know that the co-seismic electric fields induced by the MI effect are not sensitive to the rock conductivity whereas the co-seismic magnetic fields tend to increase as the conductivity increases. From Gao (2010) we know that both the co-seismic electric and magnetic fields induced by the EK effect decrease as the conductivity increases. In accordance with the results in this paper, the co-seismic electric fields arising from the PZ effect decrease as the conductivity increases. Besides, the radial and vertical components of the co-seismic magnetic fields

are not sensitive to the rock conductivity. The tangential component differs from the other two components and the greater the difference of conductivities between the shallow interfaces, the stronger the co-seismic magnetic fields. That is to say, the MI effect will dominate the EM disturbance in the stratum of high conductivities while the PZ and EK effects will dominate when the conductivity is low.

Furthermore, the studies provided in this paper suggest that the radial component of the co-seismic electric fields caused by the PZ effect is stronger than the other two components especially than the vertical component (Figs 9 and10). But, the simulations of the EK effect reveal that the vertical component of co-seismic electric fields is more than 2 orders of magnitude higher than the horizontal components (Gao, 2010; Hu & Gao, 2011). This demonstrates that the PZ and EK effects possess different characteristics in generating the co-seismic electric fields.

The piezoelectric EM responses presented in this paper are significantly related to the piezoelectric modulus ***d***. The quartz aggregates will possess '∞m' symmetry if they are composed of equal compositions of two enantiomorphs (left-hand and right-hand). Besides, *a*-axis of these two hands are antiparallel and *c*-axis are random in a plane. In the natural crust, left-hand and right-hand quartz tend to co-exist and form twined crystals, and thus '∞m' is a typical symmetry, which is adopted in this paper. Actually, the quartz aggregates might possess other symmetries, for instance, '∞', '$\infty 2$' and so on. If another symmetry is adopted, the EM responses due to the PZ effect may have different characteristics. Further study needs to be conducted to explore the possible new characteristics

4. Conclusions

In this paper, a 3D horizontal stratified model is used to study the EM fields excited by earthquakes due to the PZ effect. The coupled equations of seismic and EM waves are solved in the frequency-wavenumber domain through the Global Matrix method, then the solution in time-space domain is obtained by the Hankel transform and the inverse Fourier transform. Numerical experiments are separately carried out to investigate the characteristics of the piezoelectric EM responses.

The results show that two kinds of EM signals can be produced by the earthquake due to the PZ effect. One is the early-EM signal, including the EM wave directly generated by the source and that converted from a seismic wave at an interface. The early-EM signal starts at the moment of the earthquake eruption because the EM wave travels much faster than the seismic wave. It possesses great significance to earthquake early warning. The other is the co-seismic EM field associated with the seismic wave, which arrives at the observation synchronously with the seismic wave and carries the information of the underground medium.

The numerical experiments suggest that the P wave can produce both horizontal and vertical electric fields as well as horizontal co-seismic magnetic fields but no vertical magnetic field. Whereas the SH wave can produce both horizontal and vertical magnetic fields as well as horizontal electric fields but no vertical electric field. In addition, the EM responses generated by the fault slip source in the half-space and three-layers models show that there are co-seismic electric and magnetic signals

accompanying the Rayleigh wave. For an $M_w = 6.1$ earthquake the co-seismic electric fields reach ~10 μV/m, which can be observed by the current instrument. The co-seismic magnetic fields are ~10^{-4} nT, which are weak but still within the detectability of some precise magnetic sensors.

We analyze the sensitivity of the co-seismic EM fields to the rock conductivity. The results show that both the conductivities of the shallow layer where the receiver is located and the deep layer have impact on the co-seismic EM fields. The co-seismic electric field decreases approximately linearly with increasing shallow conductivities. The co-seismic magnetic field hardly change with the shallow conductivities unless the conductivity is fairly high ($> 0.1\,\mathrm{S/m}$).

The co-seismic EM fields might be influenced by the conductivity of the rock of the deep layer when the interface is shallow (i.e., the top layer is thin). In this case, the horizontal components of the co-seismic electric fields decrease as the conductivity of the deep layer increases, but the vertical component barely changes with the conductivity. The radial and vertical components magnetic fields barely change either as the conductivity changes except for fairly high conductivities ($> 0.1\,\mathrm{S/m}$). Besides, the tangential component of the co-seismic magnetic field associated the P wave will decrease when the conductivity of the deep layer increases. The tangential magnetic components associated with S or R waves behave differently comparing to that with the P wave. They reach the minimum when the conductivity of the deep layer is equal to that of the upper layer where the receiver is located (in this situation, the two-layers model becomes a half-space model). In other words, the tangential magnetic fields

associated with S and R waves tend to be enhanced when conductivities of the upper and the lower layers are different.

Acknowledgements

This study was supported by the National Natural Science Foundation of China (grant 42174084) and Fundamental Research Funds for the Central Universities of China (grant JZ2021HGPB0058).

Data Availability Statement

The data generated using the semi-analytical method corresponding to this study is available at https://figshare.com/s/114da2dba1c0b2ed7a06.

Appendix A. Derivation of the Analytical Expressions of the Eigenvalues and Eigenvectors of Matrix A

The coupled equations of the seismic and EM waves due to the piezoelectric effect can be decoupled into two modes of derivative equations, i.e., eq.(22) for the PSVM mode and eq.(23) for the SHTE mode, which are both equivalent to two-dimensional equations. The eigenvector of the system matrix **A** is essentially the fundamental solution of the displacement-stress-electromagnetic responses generated by the down-

and up-going waves in each layer, which can be analytically derived using the plane wave theory.

If we regard the subscripts as $S \to x$, $T \to y$ and $R \to z$, eq.(22) is equivalent to the following equations satisfied by the 2D PSVTM mode waves propagating in the *x*-*z* plane, where *x* points to the horizontal direction and *z* points to the downward direction:

$$\frac{\partial \tau_{xx}}{\partial x} + \frac{\partial \tau_{zx}}{\partial z} = -\omega^2 \rho u_x - F_x, \tag{A1}$$

$$\frac{\partial \tau_{xz}}{\partial x} + \frac{\partial \tau_{zz}}{\partial z} = -\omega^2 \rho u_z - F_z, \tag{A2}$$

$$\tau_{xx} = \left(\lambda + 2G\right)\frac{\partial u_x}{\partial x} + \lambda \frac{\partial u_z}{\partial z}, \tag{A3}$$

$$\tau_{zz} = \left(\lambda + 2G\right)\frac{\partial u_z}{\partial z} + \lambda \frac{\partial u_x}{\partial x}, \tag{A4}$$

$$\tau_{xz} = G\left(\frac{\partial u_x}{\partial z} + \frac{\partial u_z}{\partial x}\right), \tag{A5}$$

$$\frac{\partial E_x}{\partial z} - \frac{\partial E_z}{\partial x} = i\omega\mu H_y, \tag{A6}$$

$$\frac{\partial H_y}{\partial z} = i\omega\tilde{\varepsilon} E_x + i\omega p_x - J_{sx}, \tag{A7}$$

$$\frac{\partial H_y}{\partial x} = -i\omega\tilde{\varepsilon} E_z - i\omega p_z + J_{sz}. \tag{A8}$$

Eq.(23) is equivalent to the following equations satisfied by the 2D SHTE mode waves propagating in the *x*-*z* plane

$$\frac{\partial \tau_{yx}}{\partial x} + \frac{\partial \tau_{yz}}{\partial z} = -\omega^2 \rho u_y - F_y, \tag{A9}$$

$$\tau_{yz} = G\frac{\partial u_y}{\partial z}, \tag{A10}$$

$$\tau_{yx} = G\frac{\partial u_y}{\partial x}, \tag{A11}$$

$$\frac{\partial E_y}{\partial z} = -i\omega\mu H_x, \tag{A12}$$

$$\frac{\partial E_y}{\partial x} = i\omega\mu H_z, \tag{A13}$$

$$\frac{\partial H_x}{\partial z} - \frac{\partial H_z}{\partial x} = -i\omega\tilde{\varepsilon}E_y - i\omega p_y + J_{sy}. \tag{A14}$$

In addition, three components of the polarization vector **p** caused by the piezoelectric effect can be expressed as

$$p_x = -2d_0\tau_{xz}, \tag{A15}$$

$$p_y = -2d_0\tau_{yz}, \tag{A16}$$

$$p_z = -d_0\tau_{xx} + 2d_0\tau_{zz}. \tag{A17}$$

Based on the plane wave theory, we derive the fundamental solutions of the displacement-stress-electromagnetic responses of PSVTM and SHTE mode waves propagating in the *x*-*z* plane.

A.1. Displacement and Stress Fields Produced by Seismic Waves

A.1.1. Displacement and Stress Fields Produced by PSV Waves

The piezoelectric effect in the rock is not strong thus the feedback of the electromagnetic wave to seismic waves can be omitted. Therefore, the displacement and stress fields can be solved from the elastodynamic equations, namely, eqs (A1)-

(A5). Considering that the P and SV waves propagate in the *x*-*z* plane the displacement field can be expressed as

$$\mathbf{u} = \nabla\phi + \nabla\times(\psi\mathbf{e}_y), \tag{A18}$$

in which ϕ and ψ are potential functions related to the P and SV waves, respectively.

The potential functions ϕ and ψ have the plane wave solutions of the following forms (the term $e^{-i\omega t}$ is omitted for convenience)

$$\begin{cases} \phi = A^{+P}e^{ikx+i\gamma^P z} + A^{-P}e^{ikx-i\gamma^P z} \\ \psi = A^{+SV}e^{ikx+i\gamma^S z} + A^{-SV}e^{ikx-i\gamma^S z} \end{cases}, \tag{A19}$$

in which A^{+P} and A^{+SV} denote the amplitudes of the down-going P and SV waves, A^{-P} and A^{-SV} denote the amplitudes of the up-going P and SV waves. i is the imaginary unit. k is the horizontal wavenumber. γ^P and γ^S denote the vertical wavenumbers related to P and S waves, respectively.

$$\gamma^P = \sqrt{\frac{\omega^2}{V_P^2} - k^2}, \tag{A20}$$

$$\gamma^S = \sqrt{\frac{\omega^2}{V_S^2} - k^2}. \tag{A21}$$

V_P and V_S are velocities of the P and S waves. ω is the angular frequency. Substituting eq.(A19) into eq.(A18) and combining eqs (A3)-(A5) we obtain the displacement and stress fields produced by the PSV mode waves,

$$\begin{pmatrix} u_x \\ u_z \\ \tau_{xz} \\ \tau_{zz} \end{pmatrix} = \begin{pmatrix} ik & ik & -i\gamma^S & i\gamma^S \\ i\gamma^P & -i\gamma^P & ik & ik \\ -2Gk\gamma^P & 2Gk\gamma^P & G\left(\gamma^S\gamma^S - kk\right) & G\left(\gamma^S\gamma^S - kk\right) \\ -\left(\lambda k^P k^P + 2G\gamma^P\gamma^P\right) & -\left(\lambda k^P k^P + 2G\gamma^P\gamma^P\right) & -2Gk\gamma^S & 2Gk\gamma^S \end{pmatrix} \begin{pmatrix} A^{+P}e^{ikx+i\gamma^P z} \\ A^{-P}e^{ikx-i\gamma^P z} \\ A^{+SV}e^{ikx+i\gamma^S z} \\ A^{-SV}e^{ikx-i\gamma^S z} \end{pmatrix}. \tag{A22}$$

λ and G are lamé constants. k^P is the wavenumber of the P wave,

$$k^P = \frac{\omega}{V_P}. \tag{A23}$$

A.1.2. Displacement and Stress Fields Produced by SH Waves

Now that the SH wave propagates in the *x*-*z* plane, its displacement has the plane wave solutions, i.e.,

$$u_y = A^{+SH} e^{ikx+i\gamma^S z} + A^{-SH} e^{ikx-i\gamma^S z}. \tag{A24}$$

The stress field can be yielded using eq.(A10). Combining them we obtain

$$\begin{pmatrix} u_y \\ \tau_{yz} \end{pmatrix} = \begin{pmatrix} 1 & 1 \\ Gi\gamma^S & -Gi\gamma^S \end{pmatrix} \begin{pmatrix} A^{+SH} e^{ikx+i\gamma^S z} \\ A^{-SH} e^{ikx-i\gamma^S z} \end{pmatrix}. \tag{A25}$$

A^{+SH} and A^{-SH} denote the amplitudes of the down- and up-going SH waves, respectively.

A.2. Electromagnetic Fields Produced by Seismic and Electromagnetic Waves

To derive the EM fields generated by the seismic and EM waves, we introduce the scalar potential **A** of the magnetic field

$$\mathbf{H} = \frac{1}{\mu} \nabla \times \mathbf{A}, \tag{A26}$$

where μ is the magnetic permeability of the vacuum. $\nabla \times (\mathbf{E} - i\omega\mathbf{A}) = 0$ is obtained by substituting eq.(A26) into eq.(3), and then $\mathbf{E} - i\omega\mathbf{A}$ can be expressed by the gradient of a scalar φ and thus we have

$$\mathbf{E} = -\nabla\varphi + i\omega\mathbf{A}. \tag{A27}$$

Then we substitute eqs (A26) and (A27) into eq.(4), and apply the Lorentz gauge,

$$\nabla \cdot \mathbf{A} - i\omega\mu\tilde{\varepsilon}\varphi = 0. \tag{A28}$$

The electric field thus can be expressed as

$$\mathbf{E} = -\frac{\nabla\nabla\cdot\mathbf{A}}{i\omega\mu\tilde{\varepsilon}} + i\omega\mathbf{A}, \tag{A29}$$

By omitting the ambient current (i.e., $\mathbf{J}_s = 0$) we obtain the following equation

$$\nabla^2\mathbf{A} + k^{EM}k^{EM}\mathbf{A} = i\omega\mu\mathbf{p}, \tag{A30}$$

where k^{EM} is the wavenumber of the EM wave, i.e.,

$$k^{EM} = \sqrt{\omega^2\mu\tilde{\varepsilon}}, \tag{A31}$$

and **p** is the polarization vector due to the piezoelectric effect.

The solution of the inhomogeneous equation eq.(A30) can be expressed as a superposition of a particular solution and a general solution of the following homogenous equation

$$\nabla^2\mathbf{A} + k^{EM}k^{EM}\mathbf{A} = 0. \tag{A32}$$

A.2.1. Particular Solutions: EM Fields Generated by Seismic Waves

The particular solutions are caused by the polarization vector contributed by the seismic waves. Let $\mathbf{p}^P$, $\mathbf{p}^{SV}$ and $\mathbf{p}^{SH}$ be the polarization vectors contributed by P, SV and SH waves, respectively, and suppose $\mathbf{A}^P$, $\mathbf{A}^{SV}$ and $\mathbf{A}^{SH}$ be the corresponding solutions of eq.(A30), i.e.,

$$\nabla^2\mathbf{A}^P + k^{EM}k^{EM}\mathbf{A}^P = i\omega\mu\mathbf{p}^P, \tag{A33}$$

$$\nabla^2\mathbf{A}^{SV} + k^{EM}k^{EM}\mathbf{A}^{SV} = i\omega\mu\mathbf{p}^{SV}, \tag{A34}$$

$$\nabla^2\mathbf{A}^{SH} + k^{EM}k^{EM}\mathbf{A}^{SH} = i\omega\mu\mathbf{p}^{SH}. \tag{A35}$$

It is easy to verify that the following expressions

$$\mathbf{A}^P = \frac{i\omega\mu\mathbf{p}^P}{k^{EM}k^{EM} - k^Pk^P}, \tag{A36}$$

$$\mathbf{A}^{SV} = \frac{i\omega\mu\mathbf{p}^{SV}}{k^{EM}k^{EM} - k^S k^S}, \tag{A37}$$

$$\mathbf{A}^{SH} = \frac{i\omega\mu\mathbf{p}^{SH}}{k^{EM}k^{EM} - k^S k^S}, \tag{A38}$$

respectively satisfy equations (A33), (A34) and (A35), where

$$k^S = \frac{\omega}{V_S}. \tag{A39}$$

Then we obtain the electric and magnetic fields for the P, SV and SH waves,

$$\begin{cases} \mathbf{H}^P = \dfrac{i\omega}{k^{EM}k^{EM} - k^P k^P}\nabla\times\mathbf{p}^P \\ \mathbf{E}^P = -\dfrac{\nabla\nabla\cdot\mathbf{p}^P + \omega^2\tilde{\varepsilon}\mu\mathbf{p}^P}{\tilde{\varepsilon}\left(k^{EM}k^{EM} - k^P k^P\right)} \end{cases}, \tag{A40}$$

$$\begin{cases} \mathbf{H}^{SV} = \dfrac{i\omega}{k^{EM}k^{EM} - k^S k^S}\nabla\times\mathbf{p}^{SV} \\ \mathbf{E}^{SV} = -\dfrac{\nabla\nabla\cdot\mathbf{p}^{SV} + \omega^2\tilde{\varepsilon}\mu\mathbf{p}^{SV}}{\tilde{\varepsilon}\left(k^{EM}k^{EM} - k^S k^S\right)} \end{cases}. \tag{A41}$$

$$\begin{cases} \mathbf{H}^{SH} = \dfrac{i\omega}{k^{EM}k^{EM} - k^S k^S}\nabla\times\mathbf{p}^{SH} \\ \mathbf{E}^{SH} = -\dfrac{\nabla\nabla\cdot\mathbf{p}^{SH} + \omega^2\tilde{\varepsilon}\mu\mathbf{p}^{SH}}{\tilde{\varepsilon}\left(k^{EM}k^{EM} - k^S k^S\right)} \end{cases}. \tag{A42}$$

Combining eqs (A3), (A15), (A17) and (A22) we obtain $\mathbf{p}^P$

$$\begin{pmatrix} p_x^P \\ p_z^P \end{pmatrix} = -2d_0 G \begin{pmatrix} -2k\gamma^P & 2k\gamma^P \\ 2\gamma^P\gamma^P - kk & 2\gamma^P\gamma^P - kk \end{pmatrix} \begin{pmatrix} A^{+P}e^{ikx+i\gamma^P z} \\ A^{-P}e^{ikx-i\gamma^P z} \end{pmatrix}, \tag{A43}$$

and $\mathbf{p}^{SV}$

$$\begin{pmatrix} p_x^{SV} \\ p_z^{SV} \end{pmatrix} = -2d_0 G \begin{pmatrix} \gamma^S\gamma^S - kk & \gamma^S\gamma^S - kk \\ 3k\gamma^S & -3k_x\gamma^S \end{pmatrix} \begin{pmatrix} A^{+SV}e^{ikx+i\gamma^S z} \\ A^{-SV}e^{ikx-i\gamma^S z} \end{pmatrix}. \tag{A44}$$

Substituting eq.(A43) into eq.(A40) we finally obtain the plane wave solutions of the electric and magnetic fields generated by the down- and up-going P waves,

$$\mathbf{E}^P = E_x^P\mathbf{e}_x + E_z^P\mathbf{e}_z, \tag{A45}$$

$$E_x^P = \frac{2d_0 Gk\gamma^P \left(3kk - 2\gamma^P\gamma^P - 2k^{EM}k^{EM}\right)}{\tilde{\varepsilon}\left(k^{EM}k^{EM} - k^P k^P\right)}\left(A^{+P}e^{ikx+i\gamma^P z} - A^{-P}e^{ikx-i\gamma^P z}\right), \quad \text{(A46)}$$

$$E_z^P = \frac{2d_0 G\gamma^P\gamma^P \left(3kk - 2\gamma^P\gamma^P + 2k^{EM}k^{EM}\right) - 2d_0 Gkkk^{EM}k^{EM}}{\tilde{\varepsilon}\left(k^{EM}k^{EM} - k^P k^P\right)}\left(A^{+P}e^{ikx+i\gamma^P z} + A^{-P}e^{ikx-i\gamma^P z}\right), \quad \text{(A47)}$$

$$\mathbf{H}^P = H_y^P \vec{e}_y = \frac{2d_0 G\omega k\left(4\gamma^P\gamma^P - kk\right)}{k^{EM}k^{EM} - k^P k^P}\left(A^{+P}e^{ikx+i\gamma^P z} + A^{-P}e^{ikx-i\gamma^P z}\right)\vec{e}_y . \quad \text{(A48)}$$

Substituting eq.(A44) into eq.(A41) we obtain the plane wave solutions of the electric and magnetic fields generated by the down- and up-going SV waves,

$$\mathbf{E}^{SV} = E_x^{SV}\mathbf{e}_x + E_z^{SV}\mathbf{e}_z , \quad \text{(A49)}$$

where

$$E_x^{SV} = \frac{2d_0 G\left(4k^2\gamma^S\gamma^S - k^4 + k^2k^{EM}k^{EM} - \gamma^S\gamma^S k^{EM}k^{EM}\right)}{-\tilde{\varepsilon}\left(k^{EM}k^{EM} - k^S k^S\right)}\left(A^{+SV}e^{ikx+i\gamma^S z} + A^{-SV}e^{ikx-i\gamma^S z}\right) \quad ,$$

(A50)

$$E_z^{SV} = \frac{-2d_0 Gk\gamma^S \left(4\gamma^S\gamma^S - kk - 3k^{EM}k^{EM}\right)}{\tilde{\varepsilon}\left(k^{EM}k^{EM} - k^S k^S\right)}\left(A^{+SV}e^{ikx+i\gamma^S z} + A^{-SV}e^{ikx-i\gamma^S z}\right),$$

(A51)

$$\mathbf{H}^{SV} = H_y^{SV}\vec{e}_y = \frac{2d_0\omega G\gamma^S\left(4kk - \gamma^S\gamma^S\right)}{k^{EM}k^{EM} - k^S k^S}\left(A^{+SV}e^{ikx+i\gamma^S z} + A^{-SV}e^{ikx-i\gamma^S z}\right)\vec{e}_y .$$

(A52)

For the SH wave, $\mathbf{p}^{SH}$ can be yielded using eqs (A16) and (A25) in the form of the plane wave solutions, i.e.,

$$\mathbf{p}^{SH} = p_y^{SH}\mathbf{e}_y , \quad \text{(A53)}$$

where

$$p_y^{SH} = -2d_0 Gi\gamma^S\left(A^{+SH}e^{ikx+i\gamma^S z} - A^{-SH}e^{ikx-i\gamma^S z}\right). \quad \text{(A54)}$$

Then we get the EM fields generated by the down- and up-going SH waves after substituting eq.(A53) into eq.(A42),

$$\mathbf{E}^{SH} = E_y^{SH}\mathbf{e}_y = \frac{2d_0\omega^2\mu G i\gamma^S}{k^{EM}k^{EM} - k^S k^S}\left(A^{+SH}e^{ikx+i\gamma^S z} - A^{-SH}e^{ikx-i\gamma^S z}\right)\mathbf{e}_y, \tag{A55}$$

$$\mathbf{H}^{SH} = H_x^{SH}\mathbf{e}_x + H_z^{SH}\mathbf{e}_z, \tag{A56}$$

where

$$H_x^{SH} = \frac{2d_0 G i\omega\gamma^S\gamma^S}{k^{EM}k^{EM} - k^S k^S}\left(A^{+SH}e^{ikx+i\gamma^S z} + A^{-SH}e^{ikx-i\gamma^S z}\right), \tag{A57}$$

$$H_z^{SH} = \frac{-2d_0 G i\omega k\gamma^S}{k^{EM}k^{EM} - k^S k^S}\left(A^{+SH}e^{ikx+i\gamma^S z} - A^{-SH}e^{ikx-i\gamma^S z}\right). \tag{A58}$$

A.2.2. General Solution: EM Fields Due to EM Waves

We are going to derive the homogeneous general solution of eq.(A32), i.e., the EM fields generated by the EM waves. Notice that **A** in eq.(A32) is the potential function of the magnetic field only with two independent components.

Similar to eq.(A19), in terms of the EM waves traveling in the *x*-*z* plane, we take A_x and A_y as two independent components and let them possess the following plane wave solutions, i.e.,

$$\begin{cases} A_x = A^{+x}e^{ikx+i\gamma^{EM}z} + A^{-x}e^{ikx-i\gamma^{EM}z} \\ A_y = A^{+y}e^{ikx+i\gamma^{EM}z} + A^{-y}e^{ikx-i\gamma^{EM}z} \end{cases}, \tag{A59}$$

where γ^{EM} denotes the vertical wavenumber of the EM wave. Then we get the magnetic field by substituting eq.(A59) into eq.(A26),

$$\mathbf{H}=\begin{pmatrix} 0 & 0 & -\dfrac{i\gamma^{EM}}{\mu} & \dfrac{i\gamma^{EM}}{\mu} \\ \dfrac{i\gamma^{EM}}{\mu} & -\dfrac{i\gamma^{EM}}{\mu} & 0 & 0 \\ 0 & 0 & \dfrac{ik}{\mu} & \dfrac{ik}{\mu} \end{pmatrix}\begin{pmatrix} A^{+x}e^{ikx+i\gamma^{EM}z} \\ A^{-x}e^{ikx-i\gamma^{EM}z} \\ A^{+y}e^{ikx+i\gamma^{EM}z} \\ A^{-y}e^{ikx-i\gamma^{EM}z} \end{pmatrix}. \tag{A60}$$

And we obtain the electric field by combining eqs (A27), (A28) and (A32),

$$\mathbf{E}=-\frac{1}{i\omega\tilde{\varepsilon}}\nabla\times\mathbf{H}. \tag{A61}$$

Then we yield the plane wave solutions of the electric field by substituting eq.(A60) into eq.(A61),

$$\mathbf{E}=-\frac{1}{i\omega\tilde{\varepsilon}\mu}\begin{bmatrix} \left(\gamma^{EM}\right)^2 & \left(\gamma^{EM}\right)^2 & 0 & 0 \\ 0 & 0 & \left(k^{EM}\right)^2 & \left(k^{EM}\right)^2 \\ -k\gamma^{EM} & k\gamma^{EM} & 0 & 0 \end{bmatrix}\begin{pmatrix} A^{+x}e^{ikx+i\gamma^{EM}z} \\ A^{-x}e^{ikx-i\gamma^{EM}z} \\ A^{+y}e^{ikx+i\gamma^{EM}z} \\ A^{-y}e^{ikx-i\gamma^{EM}z} \end{pmatrix}. \tag{A62}$$

From eqs (A60) and (A62) we find that A^{+x} and A^{-x} are only associated with E_x, E_z and H_y, i.e., the TM wave. Therefore, we obtain the plane wave solutions of the TM wave,

$$\begin{pmatrix} E_x \\ E_z \\ H_y \end{pmatrix}=\begin{bmatrix} \gamma^{EM} & -\gamma^{EM} \\ -k & -k \\ \omega\tilde{\varepsilon} & \omega\tilde{\varepsilon} \end{bmatrix}\begin{pmatrix} A^{+TM}e^{ikx+i\gamma^{EM}z} \\ A^{-TM}e^{ikx-i\gamma^{EM}z} \end{pmatrix}. \tag{A63}$$

Similarly, A^{+y} and A^{-y} are associated with H_x, H_z and E_y, i.e., the TE wave,

$$\begin{pmatrix} E_y \\ H_x \\ H_z \end{pmatrix}=\begin{bmatrix} \omega\mu & \omega\mu \\ -\gamma^{EM} & \gamma^{EM} \\ k & k \end{bmatrix}\begin{pmatrix} A^{+TE}e^{ikx+i\gamma^{EM}z} \\ A^{-TE}e^{ikx-i\gamma^{EM}z} \end{pmatrix}, \tag{A64}$$

where A^{+TM}, A^{-TM} and A^{+TE}, A^{-TE} denote the amplitudes of the down-, up-going TM and TE waves.

A.3. Eigenvectors for the Seismic and EM Waves

Equations (A22), (A25), (A46)-(A52), (A55)-(A58) as well as (A63) and (A64) present the plane wave solutions of the displacement-stress-EM responses. From these expressions we obtain the corresponding eigenvectors of the seismic and EM waves, i.e., $\left[u_x, u_z, \tau_{xz}, \tau_{zz}, E_x, H_y\right]^T$ for the PSVTM mode:

$$\mathbf{d}^{+P} = \begin{bmatrix} ik \\ i\gamma^P \\ -2Gk\gamma^P \\ -\left(\lambda k^P k^P + 2G\gamma^P\gamma^P\right) \\ \dfrac{2d_0 Gk\gamma^P\left(3kk - 2\gamma^P\gamma^P - 2k^{EM}k^{EM}\right)}{\tilde{\varepsilon}\left(k^{EM}k^{EM} - k^P k^P\right)} \\ \dfrac{2d_0 G\omega k\left(4\gamma^P\gamma^P - kk\right)}{k^{EM}k^{EM} - k^P k^P} \end{bmatrix}, \tag{A65}$$

$$\mathbf{d}^{-P} = \begin{bmatrix} ik \\ -i\gamma^P \\ 2Gk\gamma^P \\ -\left(\lambda k^P k^P + 2G\gamma^P\gamma^P\right) \\ -\dfrac{2d_0 Gk\gamma^P\left(3kk - 2\gamma^P\gamma^P - 2k^{EM}k^{EM}\right)}{\tilde{\varepsilon}\left(k^{EM}k^{EM} - k^P k^P\right)} \\ \dfrac{2d_0 G\omega k\left(4\gamma^P\gamma^P - kk\right)}{k^{EM}k^{EM} - k^P k^P} \end{bmatrix}, \tag{A66}$$

$$\mathbf{d}^{+SV} = \begin{bmatrix} -i\gamma^S \\ ik \\ G\left(\gamma^S\gamma^S - k^2\right) \\ -2Gk\gamma^S \\ \dfrac{2d_0 G\left(4k^2\gamma^S\gamma^S - k^4 + k^2 k^{EM}k^{EM} - \gamma^S\gamma^S k^{EM}k^{EM}\right)}{-\tilde{\varepsilon}\left(k^{EM}k^{EM} - k^S k^S\right)} \\ \dfrac{2d_0\omega G\gamma^S\left(4k^2 - \gamma^S\gamma^S\right)}{k^{EM}k^{EM} - k^S k^S} \end{bmatrix}, \tag{A67}$$

$$\mathbf{d}^{-SV}=\begin{bmatrix} i\gamma^S \\ ik \\ G\left(\gamma^S\gamma^S-k^2\right) \\ 2Gk\gamma^S \\ \dfrac{2d_0G\left(4k^2\gamma^S\gamma^S-k^4+k^2k^{EM}k^{EM}-\gamma^S\gamma^Sk^{EM}k^{EM}\right)}{-\tilde{\varepsilon}\left(k^{EM}k^{EM}-k^Sk^S\right)} \\ \dfrac{2d_0\omega G\gamma^S\left(4k^2-\gamma^S\gamma^S\right)}{k^{EM}k^{EM}-k^Sk^S} \end{bmatrix}, \tag{A68}$$

$$\mathbf{d}^{+TM}=\begin{bmatrix} 0, & 0, & 0, & 0, & \dfrac{\gamma^{EM}}{\omega\tilde{\varepsilon}}, & 1 \end{bmatrix}^T \tag{A69}$$

and

$$\mathbf{d}^{-TM}=\begin{bmatrix} 0, & 0, & 0, & 0, & -\dfrac{\gamma^{EM}}{\omega\tilde{\varepsilon}}, & 1 \end{bmatrix}^T. \tag{A70}$$

And the corresponding eigenvectors of the seismic and EM waves, i.e., $\left[u_y,\tau_{yz},E_y,H_x\right]^T$ for the SHTE mode:

$$\mathbf{d}^{+SH}=\begin{bmatrix} 1 \\ Gi\gamma^S \\ \dfrac{2d_0\omega^2\mu Gi\gamma^S}{k^{EM}k^{EM}-k^Sk^S} \\ \dfrac{2d_0Gi\omega\gamma^S\gamma^S}{k^{EM}k^{EM}-k^Sk^S} \end{bmatrix}, \tag{A71}$$

$$\mathbf{d}^{-SH}=\begin{bmatrix} 1 \\ -Gi\gamma^S \\ -\dfrac{2d_0\omega^2\mu Gi\gamma^S}{k^{EM}k^{EM}-k^Sk^S} \\ \dfrac{2d_0Gi\omega\gamma^S\gamma^S}{k^{EM}k^{EM}-k^Sk^S} \end{bmatrix}, \tag{A72}$$

$$\mathbf{d}^{+TE}=\begin{bmatrix} 0 & 0 & -\dfrac{\omega\mu}{\gamma^{EM}} & 1 \end{bmatrix}^T \tag{A73}$$

and

$$\mathbf{d}^{-TE}=\begin{bmatrix}0 & 0 & \dfrac{\omega\mu}{\gamma^{EM}} & 1\end{bmatrix}^{T}. \tag{A74}$$

Appendix B. The Derivation of the Source Term

Here we derive the expressions of the source term **S** in the cartesian coordinate system. Since this paper focuses on the electromagnetic anomalies caused by earthquakes, the influence of the external current source on the calculation is not considered here, hence we omit **J** in the following derivation.

B.1. The Derivation of the Point Source Term

We first present the expressions of the body force density **f** of the point source in the cylindrical coordinate system, i.e.,

$$\begin{cases} f_r=\left(f_{x0}\cos\theta+f_{y0}\sin\theta\right)\dfrac{\delta(r)}{r}\delta(\theta)\delta\left(z-z_0\right) \\ f_\theta=\left(f_{y0}\cos\theta-f_{x0}\sin\theta\right)\dfrac{\delta(r)}{r}\delta(\theta)\delta\left(z-z_0\right), \\ f_z=f_{z0}\dfrac{\delta(r)}{r}\delta(\theta)\delta\left(z-z_0\right) \end{cases} \tag{B1}$$

where $\delta(x)$ is the Dirac Function, f_{x0}, f_{y0} and f_{z0} are three components of the body force density in cartesian coordinates.

Substitute eq.(B1) into the surface harmonic coordinate transformation formula, i.e., eq.(11), we have

$$\begin{cases} f_{S,m}(z,k) = \int_0^{2\pi}\int_0^{+\infty} \vec{f}(r,\theta,z)\cdot\left[\vec{S}_k^m(r,\theta)\right]^* r\mathrm{d}r\mathrm{d}\theta \\ f_{T,m}(z,k) = \int_0^{2\pi}\int_0^{+\infty} \vec{f}(r,\theta,z)\cdot\left[\vec{T}_k^m(r,\theta)\right]^* r\mathrm{d}r\mathrm{d}\theta \\ f_{R,m}(z,k) = \int_0^{2\pi}\int_0^{+\infty} \vec{f}(r,\theta,z)\cdot\left[\vec{R}_k^m(r,\theta)\right]^* r\mathrm{d}r\mathrm{d}\theta \end{cases}. \tag{B2}$$

Notice that there are only three values of *m* in the above equations, $m = 0$ and ± 1. The source term **S** thus can be determined through the body force density **f**,

$$\mathbf{S} = \mathbf{f}_1 + \boldsymbol{A}\mathbf{f}_2 , \tag{B3}$$

where $\boldsymbol{A}$ is eq.(27) or eq.(30) for PSVTM or SHTE mode of waves correspondingly.

Finally, we obtain the expressions of the source term for PSVTM and SHTE modes of waves in the Cartesian coordinate system:

$$\mathbf{S}^{PSV} = -\begin{pmatrix} 0 \\ 0 \\ \left(\frac{1}{2}if_{x0} + \frac{1}{2}f_{y0}\right)\delta_{m,1} + \left(-\frac{1}{2}if_{x0} + \frac{1}{2}f_{y0}\right)\delta_{m,-1} \\ f_{z0}\delta_{m,0} \\ 0 \\ 0 \end{pmatrix}, \tag{B4}$$

$$\mathbf{S}^{SH} = -\begin{pmatrix} 0 \\ \left(\frac{1}{2}f_{x0} - \frac{1}{2}if_{y0}\right)\delta_{m,1} + \left(\frac{1}{2}f_{x0} + \frac{1}{2}if_{y0}\right)\delta_{m,-1} \\ 0 \\ 0 \end{pmatrix}. \tag{B5}$$

B.2. The Derivation of the Seismic Moment Tensor Source Term

Similar to B.1, we initially present the expressions of the seismic moment tensor source in the cylindrical coordinate system,

$$\begin{bmatrix} M_{rr} & M_{r\theta} & M_{rz} \\ M_{\theta r} & M_{\theta\theta} & M_{\theta z} \\ M_{zr} & M_{z\theta} & M_{zz} \end{bmatrix} = \begin{bmatrix} \cos\theta & \sin\theta & 0 \\ -\sin\theta & \cos\theta & 0 \\ 0 & 0 & 1 \end{bmatrix} \begin{bmatrix} M_{xx} & M_{xy} & M_{xz} \\ M_{yx} & M_{yy} & M_{yz} \\ M_{zx} & M_{zy} & M_{zz} \end{bmatrix} \begin{bmatrix} \cos\theta & -\sin\theta & 0 \\ \sin\theta & \cos\theta & 0 \\ 0 & 0 & 1 \end{bmatrix}, \tag{B6}$$

and the relationship between the moment tensor and the body force density,

$$\mathbf{F} = -\boldsymbol{M} \cdot \nabla \delta(\mathbf{r} - \mathbf{r}_0). \tag{B7}$$

Substitute the above two equations into eq.(B2), and notice $m = 0, \pm 1, \pm 2$ here. Then we get the expressions of the moment tensor source term in the cartesian coordinate system after combining eq.(B3) and some derivations.

The PSVTM mode source term:

$$\boldsymbol{S}^{PSVTM} = \begin{pmatrix} \frac{i}{2G} M_{xz}\left(\delta_{m,1} - \delta_{m,-1}\right) + \frac{1}{2G} M_{yz}\left(\delta_{m,1} + \delta_{m,-1}\right) \\ \frac{1}{\lambda + 2G} M_{zz} \delta_{m,0} \\ \frac{ik}{2}\left(M_{xx} + M_{yy} - \frac{2\lambda}{\lambda + 2G} M_{zz}\right)\delta_{m,0} + \frac{ik}{4}\left(M_{yy} - M_{xx}\right)\left(\delta_{m,2} + \delta_{m,-2}\right) + \frac{k}{4}\left(M_{xy} + M_{yx}\right)\left(\delta_{m,-2} - \delta_{m,2}\right) \\ \frac{k}{2}\left(M_{xz} - M_{zx}\right)\left(\delta_{m,1} - \delta_{m,-1}\right) + \frac{ik}{2}\left(M_{zy} - M_{yz}\right)\left(\delta_{m,1} + \delta_{m,-1}\right) \\ -\frac{4 d_0 ikG}{\tilde{\varepsilon}\left(\lambda + 2G\right)} M_{zz} \delta_{m,0} \\ d_0 \omega M_{xz}\left(\delta_{m,-1} - \delta_{m,1}\right) + i d_0 \omega M_{yz}\left(\delta_{m,1} + \delta_{m,-1}\right) \end{pmatrix}, \tag{B8}$$

and the SHTE mode source term:

$$\boldsymbol{S}^{SHTE} = \begin{pmatrix} \frac{1}{2G} M_{xz}\left(\delta_{m,1} + \delta_{m,-1}\right) + \frac{i}{2G} M_{yz}\left(\delta_{m,-1} - \delta_{m,1}\right) \\ \frac{k}{4}\left(M_{xx} - M_{yy}\right)\left(\delta_{m,-2} - \delta_{m,2}\right) + \frac{ik}{4} M_{xy}\left(\delta_{m,2} + \delta_{m,-2} + 2\delta_{m,0}\right) + \frac{ik}{4} M_{yx}\left(\delta_{m,2} + \delta_{m,-2} - 2\delta_{m,0}\right) \\ 0 \\ -id_0\omega M_{xz}\left(\delta_{m,1} + \delta_{m,-1}\right) + d_0\omega M_{yz}\left(\delta_{m,-1} - \delta_{m,1}\right) \end{pmatrix}. \quad \text{(B9)}$$

References

Azeez, K. K. A., C. Manoj, K. Veeraswamy, and T. Harinarayana (2009), Co-seismic EM signals in magnetotelluric measurement-a case study during Bhuj earthquake (26th January 2001), India, *Earth Planets and Space*, *61*(8), 973-981, doi:10.1186/bf03352947.

Bishop, J. R. (1981a), Estimating quartz fabrics from piezoelectric measurements, *Journal of the International Association for Mathematical Geology*, *13*(4), 261-289, doi:10.1007/BF01031514.

Bishop, J. R. (1981b), Piezoelectric effects in quartz-rich rocks, *Tectonophysics*, *77*(3), 297-321, doi:https://doi.org/10.1016/0040-1951(81)90268-7.

Chen, X. (1999), Seismogram synthesis in multi-layered half-space Part I. Theoretical formulations, *Earthquake Research in China*, *13*, 149-174.

Finkelstein, D., R. D. Hill, and J. R. Powell (1973), The piezoelectric theory of earthquake lightning, *Journal of Geophysical Research*, *78*(6), 992-993, doi:10.1029/JC078i006p00992.

Fitterman, D. V. (1979), Theory of electrokinetic-magnetic anomalies in a faulted half-space, *Journal of Geophysical Research*, *84*(B11), 6031-6040, doi:10.1029/JB084iB11p06031.

Gao, Y. (2010), Simulation of earthquake-induced electromagnetic wave field due to the electrokinetic effect, PHD Thesis thesis, 157 pp, Harbin Institute of Technology, Haibin, China.

Gao, Y., X. Chen, H. Hu, J. Wen, J. Tang, and G. Fang (2014), Induced electromagnetic field by seismic waves in Earth's magnetic field, *Journal of Geophysical Research-Solid Earth*, *119*(7), 5651-5685, doi:10.1002/2014jb010962.

Gao, Y., X. Chen, H. Hu, and J. Zhang (2013), Early electromagnetic waves from earthquake rupturing: I. theoretical formulations, *Geophysical Journal International*, *192*(3), 1288-1307, doi:10.1093/gji/ggs096.

Gao, Y., J. M. Harris, J. Wen, Y. Huang, C. Twardzik, X. Chen, and H. Hu (2016), Modeling of the coseismic electromagnetic fields observed during the 2004 M-w 6.0

Parkfield earthquake, *Geophysical Research Letters*, *43*(2), 620-627, doi:10.1002/2015gl067183.

Gao, Y., and H. Hu (2010), Seismoelectromagnetic waves radiated by a double couple source in a saturated porous medium, *Geophysical Journal International*, *181*(2), 873-896, doi:10.1111/j.1365-246X.2010.04526.x.

Gao, Y., D. Wang, J. Wen, H. Hu, X. Chen, and C. Yao (2019), Electromagnetic responses to an earthquake source due to the motional induction effect in a 2-D layered model, *Geophysical Journal International*, *219*(1), 563-593, doi:10.1093/gji/ggz303.

Gernets, A. A., M. V. Makarets, S. V. Koshevaya, V. V. Grimalsky, D. J. Romero, and A. N. Kotsarenko (2004), Electromagnetic emission caused by the fracturing of piezoelectric crystals with an arbitrarily oriented moving crack, *Physics and Chemistry of the Earth*, *29*(4-9), 463-472, doi:10.1016/j.pce.2003.12.006.

Gershenzon, N. I., M. B. Gokhberg, and S. L. Yunga (1993), On the electromagnetic field of an earthquake focus, *Physics of the Earth and Planetary Interiors*, *77*(1-2), 13-19, doi:10.1016/0031-9201(93)90030-d.

Ghomshei, M., B. Narod, T. L. Templeton, A. Arrott, and R. Russell (1988), Piezoelectric Pole Figure of a Vein Quartz Sample, *Textures and Microstructures*, *7*, doi:10.1155/TSM.7.303.

Ghomshei, M. M., and T. L. Templeton (1989), Piezoelectric and a-axes fabric along a quartz vein, *Physics of the Earth and Planetary Interiors*, *55*(3), 374-386, doi:https://doi.org/10.1016/0031-9201(89)90084-8.

Haartsen, M. W., and S. R. Pride (1997), Electroseismic waves from point sources in layered media, *Journal of Geophysical Research*, *102*(B11), 24745-24769, doi:10.1029/97jb02936.

Honkura, Y., et al. (2000), Preliminary results of multidisciplinary observations before, during and after the Kocaeli (Izmit) earthquake in the western part of the North Anatolian Fault Zone, *Earth, Planets and Space*, *52*(4), 293-298, doi:10.1186/bf03351638.

Hu, H., and Y. Gao (2011), Electromagnetic field generated by a finite fault due to electrokinetic effect, *Journal of Geophysical Research-Solid Earth*, *116*, doi:10.1029/2010jb007958.

Ikeya, M., S. Takaki, H. Matsumoto, A. Tani, and T. Komatsu (1997), Pulsed charge model of fault behavior producing seismic electric signals (SES), *J. Circuits Syst. Comput. (Singapore)*, *7*(3), 153-164, doi:10.1142/s0218126697000115.

Ishido, T., and H. Mizutani (1981), Experimental and theoretical basis of electrokinetic phenomena in rock-water systems and its applications to geophysics, *Journal of Geophysical Research*, *86*(B3), 1763-1775, doi:10.1029/JB086iB03p01763.

Iyemori, T., T. Kamei, Y. Tanaka, M. Takeda, T. Hashimoto, T. Araki, T. Okamoto, K. Watanabe, N. Sumitomo, and N. Oshiman (1996), Co-seismic geomagnetic variations observed at the 1995 Hyogoken-Nanbu earthquake, *Journal of Geomagnetism and Geoelectricity*, *48*(8), 1059-1070, doi:10.5636/jgg.48.1059.

Johnston, M. J., and R. J. Mueller (1987), Seismomagnetic observation during the 8 july 1986 magnitude 5.9 north palm springs earthquake, *Science (New York, N.Y.)*, *237*(4819), 1201-1203, doi:10.1126/science.237.4819.1201.

Karakelian, D., G. C. Beroza, S. L. Klemperer, and A. C. Fraser-Smith (2002), Analysis of ultralow-frequency electromagnetic field measurements associated with the 1999 M 7.1 Hector Mine, California, earthquake sequence, *Bulletin of the Seismological Society of America*, *92*(4), 1513-1524, doi:10.1785/0120000919.

Kennett, F. L. N., and N. J. Kerry (1979), Seismic waves in a stratified half space, *Geophysical Journal of the Royal Astronomical Society*, *57*(3), 557-583, doi:10.1111/j.1365-246X.1979.tb06779.x.

Matsushima, M., et al. (2002), Seismoelectromagnetic effect associated with the Izmit earthquake and its aftershocks, *Bulletin of the Seismological Society of America*, *92*(1), 350-360, doi:10.1785/0120000807.

Nitsan, U. (1977), Electromagnetic emission accompanying fracture of quartz-bearing rocks, *Geophysical Research Letters*, *4*(8), 333-336, doi:10.1029/GL004i008p00333.

Ogawa, T., and H. Utada (2000a), Coseismic piezoelectric effects due to a dislocation. 1. An analytic far and early-time field solution in a homogeneous whole space, *Physics of the Earth and Planetary Interiors*, *121*(3-4), 273-288, doi:10.1016/s0031-9201(00)00177-1.

Ogawa, T., and H. Utada (2000b), Electromagnetic signals related to incidence of a teleseismic body wave into a subsurface piezoelectric body, *Earth, Planets and Space*, *52*(4), 253-260, doi:10.1186/bf03351634.

Okawa, T., K. Oike, and T. Miura (1985), Electromagnetic radiations from rocks, *Journal of Geophysical Research*, *90*(D4), 6245-6249, doi:10.1029/JD090iD04p06245.

Okubo, K., N. Takeuchi, M. Utsugi, K. Yumoto, and Y. Sasai (2011), Direct magnetic signals from earthquake rupturing: Iwate-Miyagi earthquake of M 7.2, Japan, *Earth Planet. Sci. Lett.*, *305*(1-2), 65-72, doi:10.1016/j.epsl.2011.02.042.

Pride (1994), Governing equations for the coupled electromagnetics and acoustics of porous media, *Physical review. B, Condensed matter*, *50*(21), 15678-15696, doi:10.1103/PhysRevB.50.15678.

Qinghua, H. (2002), One possible generation mechanism of co-seismic electric signals, *Proceedings of the Japan Academy, Series B (Physical and Biological Sciences)*, *78*(7), 173-178, doi:10.2183/pjab.78.173.

Ren, H., Q. Huang, and X. Chen (2016), Existence of evanescent electromagnetic waves resulting from seismoelectric conversion at a solid-porous interface, *Geophysical Journal International*, *204*(1), 147-166, doi:10.1093/gji/ggv400.

Rikitake, T. (1968), Geomagnetism and earthquake prediction, *Tectonophysics*, *6*(1), 59-68, doi:https://doi.org/10.1016/0040-1951(68)90026-7.

Russell, R. D., M. Maxwell, K. E. Butler, and A. W. Kepic (1992), Electromagnetic Responses from Seismically Excited Targets A: Piezoelectric Phenomena at Humboldt, Australia, *Exploration Geophysics*, *23*(1-2), 281-285, doi:10.1071/EG992281.

Sasai, Y. (1991), Tectonomagnetic modeling on the basis of the linear piezomagnetic effect, *Bull. Earthq. Res. Inst. Univ. Tokyo (Japan)*, *66*(4), 585-722.

Sasaoka, H., C. Yamanaka, and M. Ikeya (1998), Measurements of electric potential variation by piezoelectricity of granite, *Geophysical Research Letters*, *25*(12), 2225-2228, doi:10.1029/98gl51179.

Sornette, A., and D. Sornette (1990), Earthquake rupture as a critical point: consequences for telluric precursors, *Tectonophysics*, *179*(3-4), 327-334, doi:10.1016/0040-1951(90)90298-m.

Stacey, F. D. (1964), The seismomagnetic effect, *pure and applied geophysics*, *58*(1), 5-22, doi:10.1007/BF00879136.

Stuart, W. D., P. O. Banks, Y. Sasai, and L. Shu-Wang (1995), Piezomagnetic field for Parkfield fault model, *Journal of Geophysical Research*, *100*(B12), 24101-24110, doi:10.1029/95jb02516.

Takeuchi, A., and H. Nagahama (2002), Interpretation of charging on fracture or frictional slip surface of rocks, *Physics of the Earth and Planetary Interiors*, *130*(3-4), 285-291, doi:10.1016/s0031-9201(02)00013-4.

Takeuchi, A., and H. Nagahama (2006), Electric dipoles perpendicular to a stick-slip plane, *Physics of the Earth and Planetary Interiors*, *155*(3-4), 208-218, doi:10.1016/j.pepi.2005.12.010.

Tang, J., Y. Zhan, L.-F. Wang, Z.-Y. Dong, G.-Z. Zhao, and J.-L. Xu (2010), Electromagnetic coseismic effect associated with aftershock of Wenchuan M(s)8.0 earthquake, *Chinese Journal of Geophysics-Chinese Edition*, *53*(3), 526-534, doi:10.3969/j.issn.0001-5733.2010.03.006.

Tuck, G. J., F. D. Stacey, and J. Starkey (1977), A search for the piezoelectric effect in quartz-bearing rocks, *Tectonophysics*, *39*(4), T7-T11, doi:https://doi.org/10.1016/0040-1951(77)90148-2.

Wang, J. H. (2021), Piezoelectricity as a mechanism on generation of electromagnetic precursors before earthquakes, *Geophysical Journal International*, *224*(1), 682-700, doi:10.1093/gji/ggaa429.

Wei, M. H., D. Z. Song, X. Q. He, Z. L. Li, L. M. Qiu, and Q. Lou (2020), Effect of Rock Properties on Electromagnetic Radiation Characteristics Generated by Rock Fracture During Uniaxial Compression, *Rock Mechanics and Rock Engineering*, *53*(11), 5223-5238, doi:10.1007/s00603-020-02216-x.

Yamazaki, K. i. (2011), Enhancement of co-seismic piezomagnetic signals near the edges of magnetization anomalies in the Earth's crust, *Earth Planets and Space*, *63*(2), 111-118, doi:10.5047/eps.2010.12.001.

Yavorovich, L. V., A. A. Bespalko, P. I. Fedotov, and R. B. Baksht (2016), Electromagnetic Radiation Generated by Acoustic Excitation of Rock Samples, *Acta Geophysica*, *64*(5), 1446-1461, doi:10.1515/acgeo-2016-0081.

Yoshida, S., and T. Ogawa (2004), Electromagnetic emissions from dry and wet granite associated with acoustic emissions, *Journal of Geophysical Research-Solid Earth*, *109*(B9), doi:10.1029/2004jb003092.

Yoshida, S., M. Uyeshima, and M. Nakatani (1997), Electric potential changes associated with slip failure of granite: preseismic and coseismic signals, *Journal of Geophysical Research*, *102*(B7), 14883-14897, doi:10.1029/97jb00729.

Zhao, J., Y. Gao, J. Tang, S. L. Klemperer, J. Wen, C.-H. Chen, and J. Chong (2021), Electromagnetic Field Generated by an Earthquake Source Due to Motional Induction in 3D Stratified Media, and Application to 2008 Mw 6.1 Qingchuan Earthquake, *Journal of Geophysical Research: Solid Earth*, *126*(10), e2021JB022102, doi:https://doi.org/10.1029/2021JB022102.

Zlotnicki, J., and F. H. Cornet (1986), A numerical model of earthquake-induced piezomagnetic anomalies, *Journal of Geophysical Research*, *91*(B1), 709-718, doi:10.1029/JB091iB01p00709.

Tables and Figures

Table 1
Parameters of the Solid Rocks

Parameter	Variable (unit)	Rock 1	Rock 2	Rock 3	Rock A
Density	ρ (g/cm^3)	2.2	2.5	2.8	2.8
Velocity of P wave	V_p (km/s)	5.1	5.9	6.5	6.5
Velocity of S wave	V_s (km/s)	3.0	3.5	3.9	3.9
Conductivity	σ (S/m)	0.01	0.01	0.01	0.001
Permittivity	ε (F/m)×10^{-10}	6.2	6.2	6.2	6.2
Permeability	μ (H/m)×10^{-7}	4π	4π	4π	4π
Thickness	h (km)	2	7	/	/

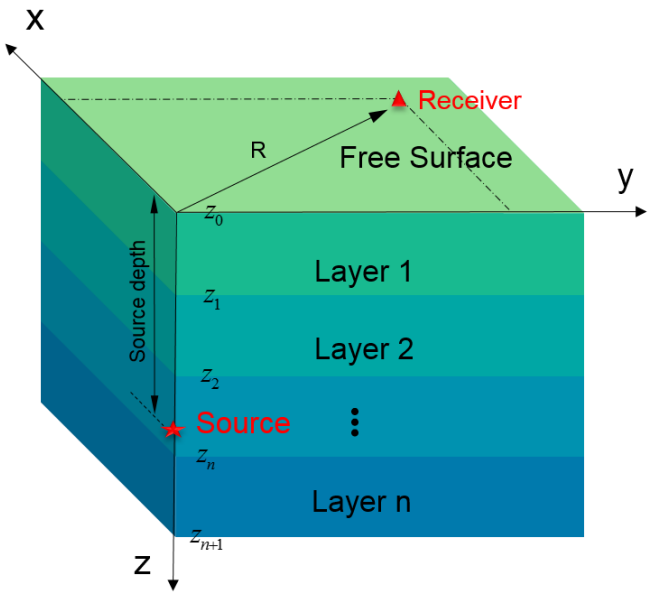

Figure 1. The schematic diagram of the 3-D horizontally layered model. *x*-, *y*- and *z*-axes denote northward, eastward and downward directions, respectively.

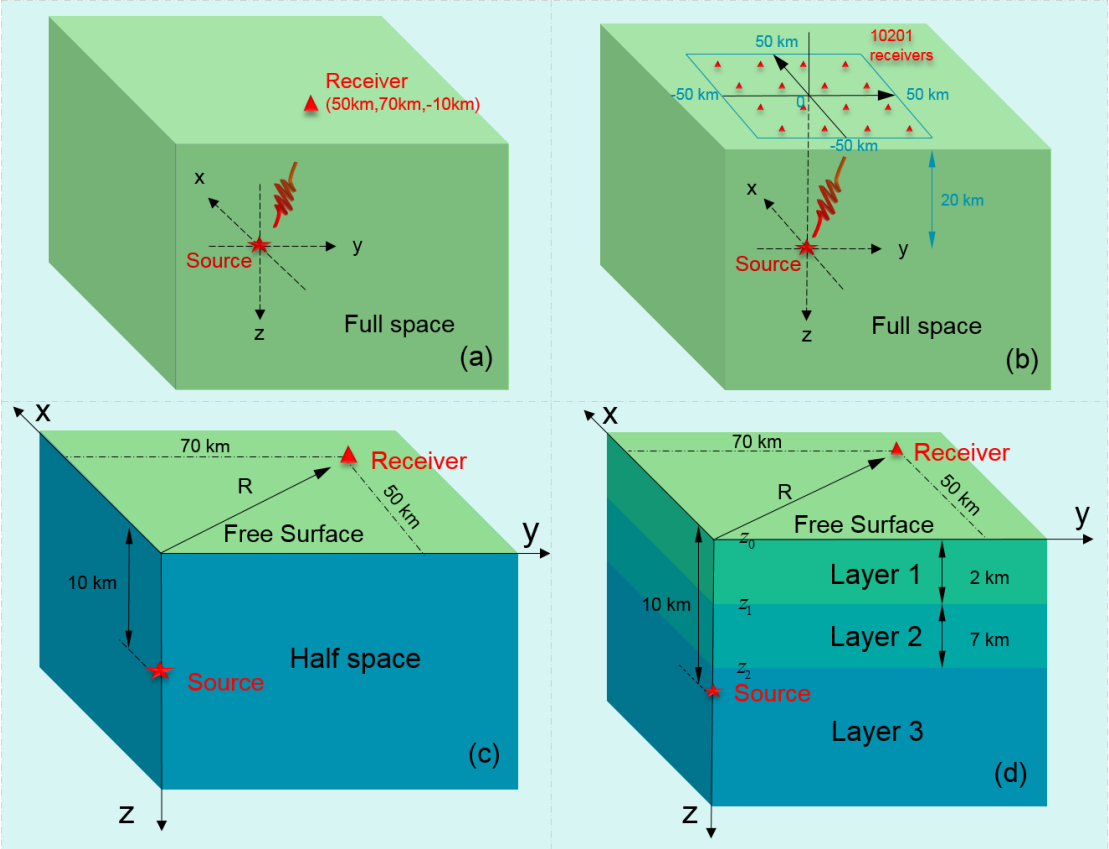

Figure 2. Schematic diagrams of the simulation models. (a) and (b) are full-space models; (c) half-space model; (d) three-layers model. A rectangular array of 10201 receivers is arranged on a plane perpendicular to z-axis in (b), which is used to observe the direct EM wave generated by the source. The depths of the receivers are 0.1m in (c) and (d).

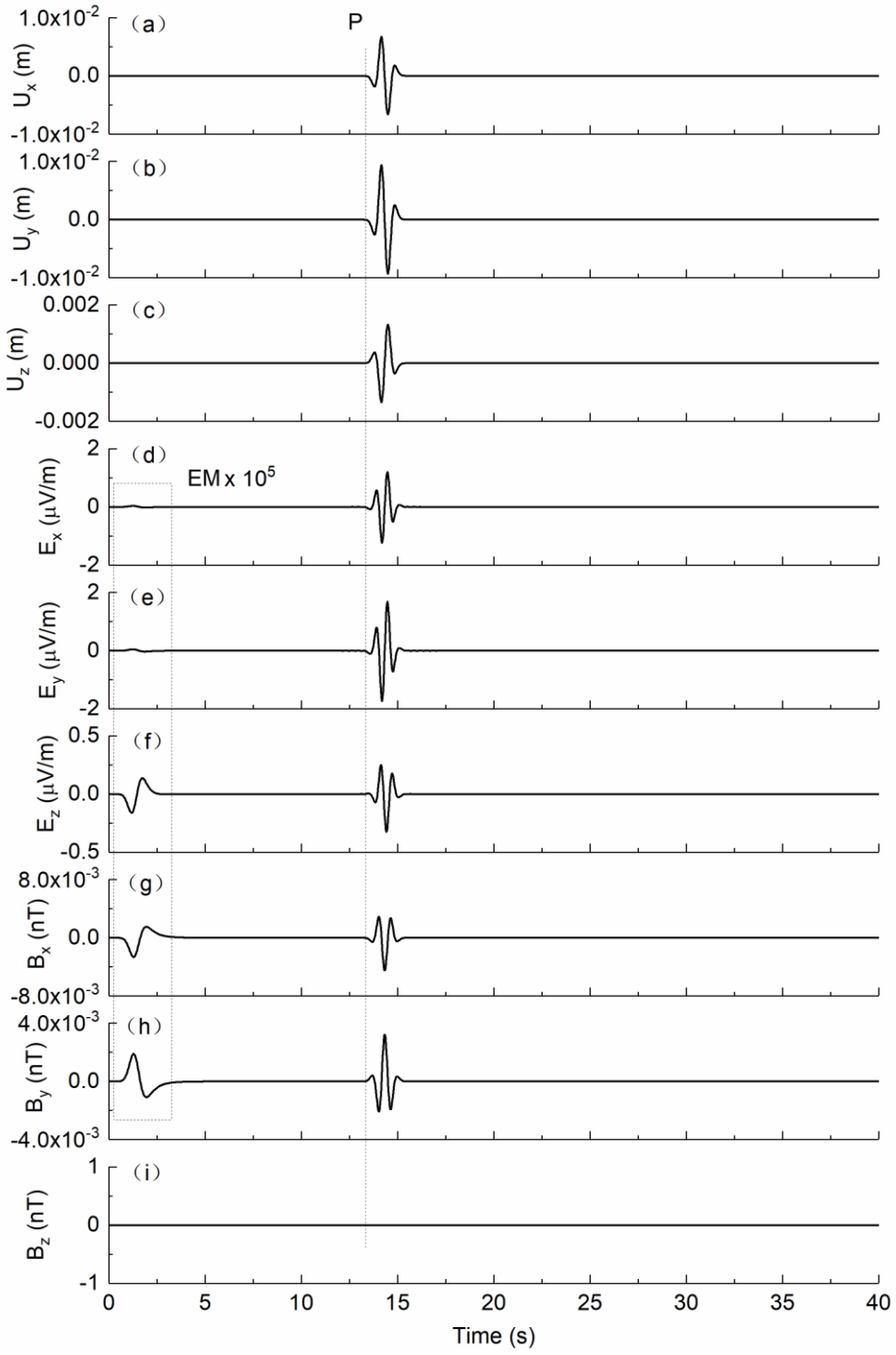

Figure 3. Seismic and EM wavefields generated by an explosive source in a full-space model. (a) - (c) are three components of the displacement field; (d) - (f) are three components of the electric field; (g) - (i) are three components of the magnetic field. The direct EM waves are amplified 10^5 times.

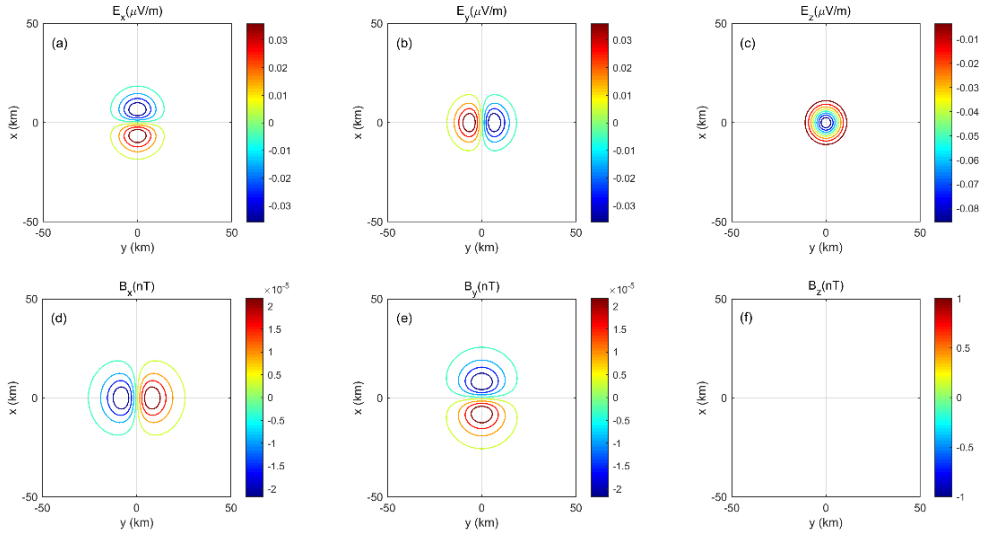

Figure 4. The amplitudes distribution in a horizontal plane of the direct EM waves generated by the explosive source. (a) - (c) are three components of the electric field; (d) - (f) are three components of the magnetic field.

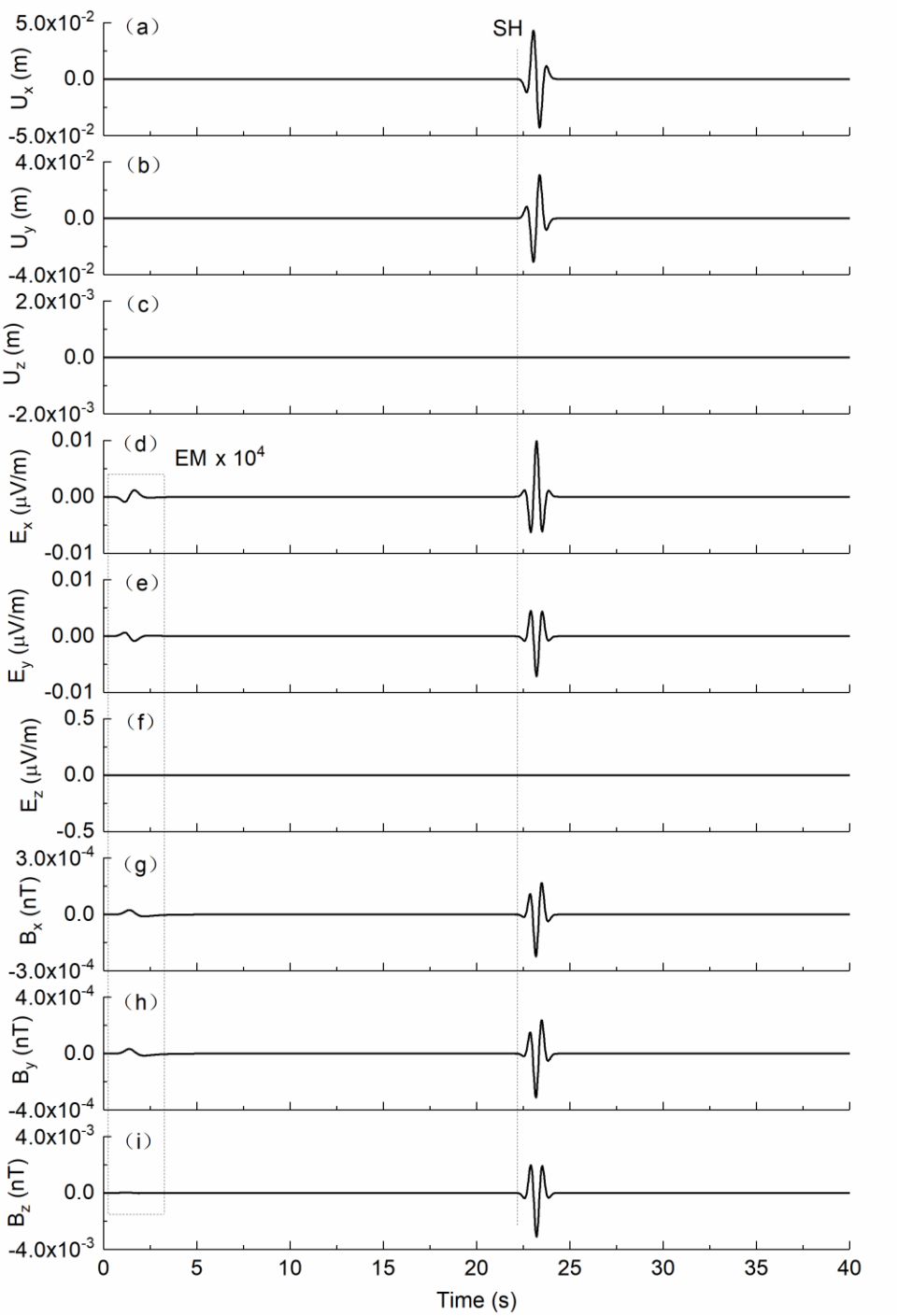

Figure 5. Seismic and EM wavefields generated by a center of rotation source in a full-space model. (a) - (c) are three components of the displacement field; (d) - (f) are three components of the electric field; (g) - (i) are three components of the magnetic field. The direct EM waves are amplified 10^4 times.

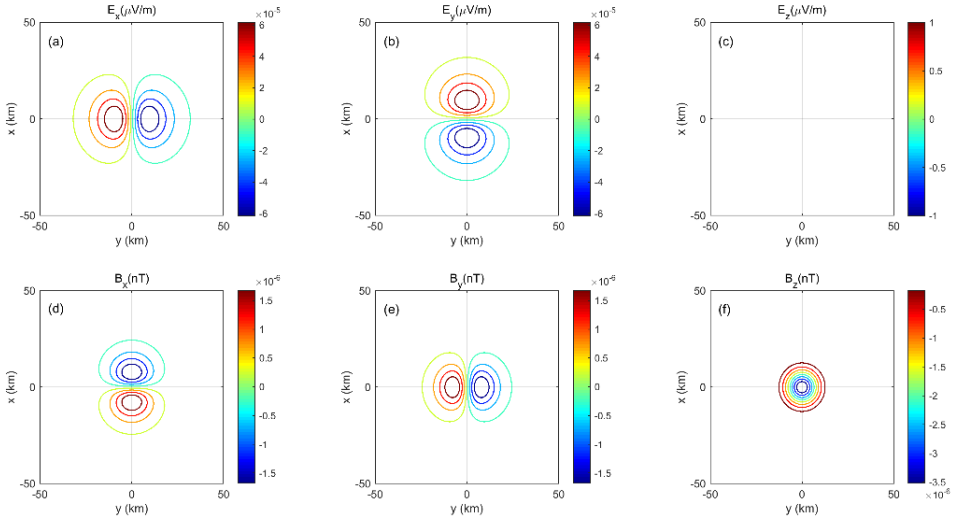

Figure 6. The amplitude distribution of the direct EM wave in a horizontal plane generated from the SH source. (a) - (c) are three components of the radiated electric field; (d) - (f) are three components of the radiated magnetic field.

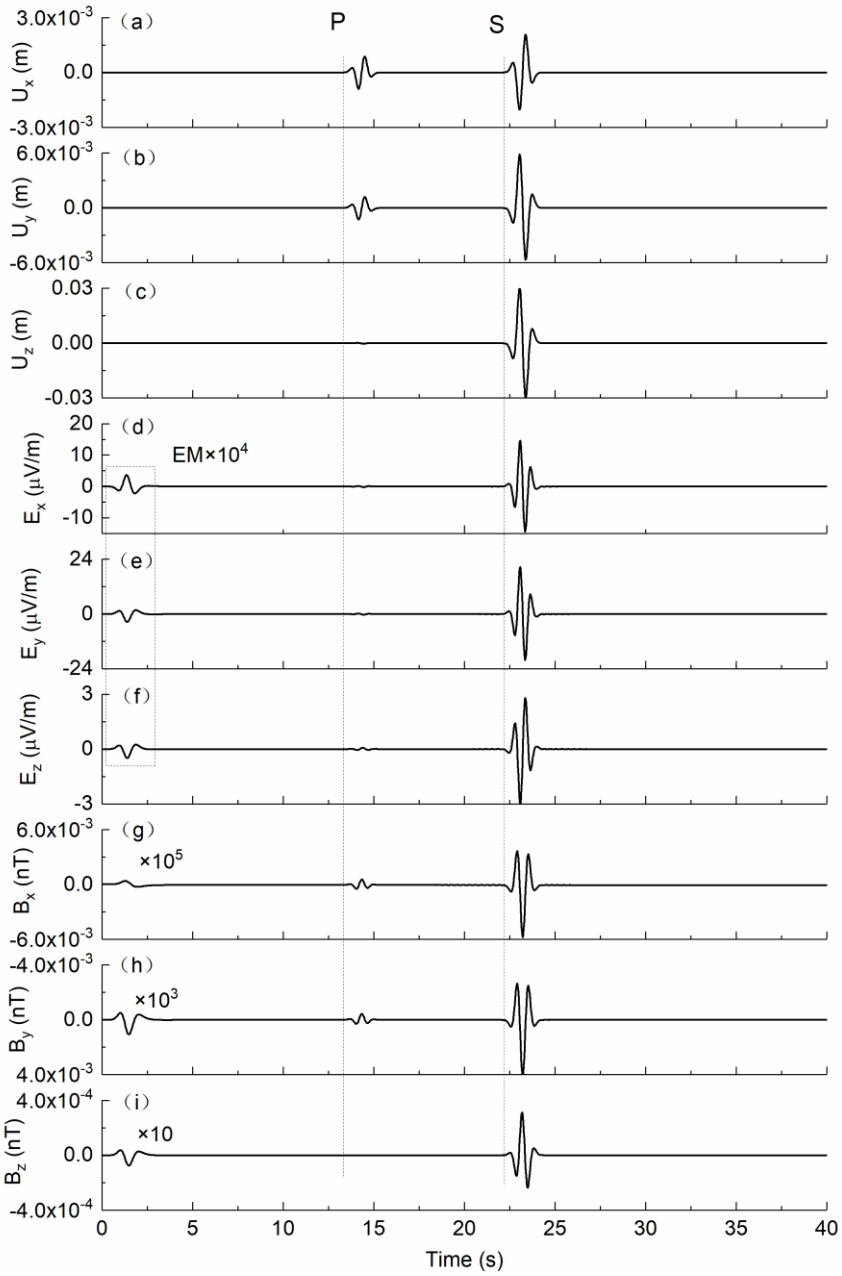

Figure 7. Seismic and EM wavefields generated by a fault slip source. (a) - (c) are three components of the displacement field; (d) - (f) are three components of the electric field; (g) - (i) are three components of the magnetic field. The direct EM wave is amplified by different coefficients for different components.

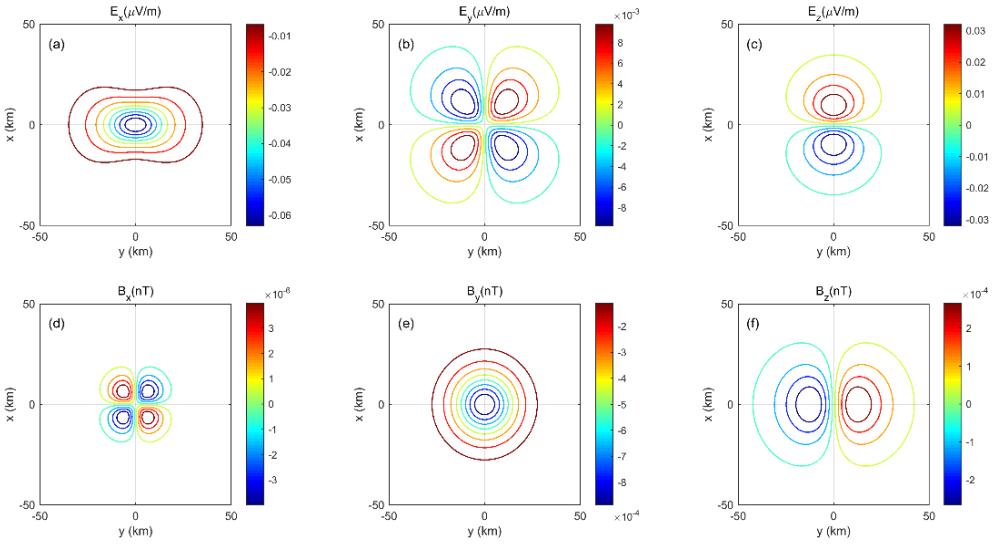

Figure 8. The amplitude distribution in a horizontal plane of the direct EM waves generated by the fault slip source. (a) - (c) are three components of the electric fields; (d) ; (f) are three components of the magnetic fields.

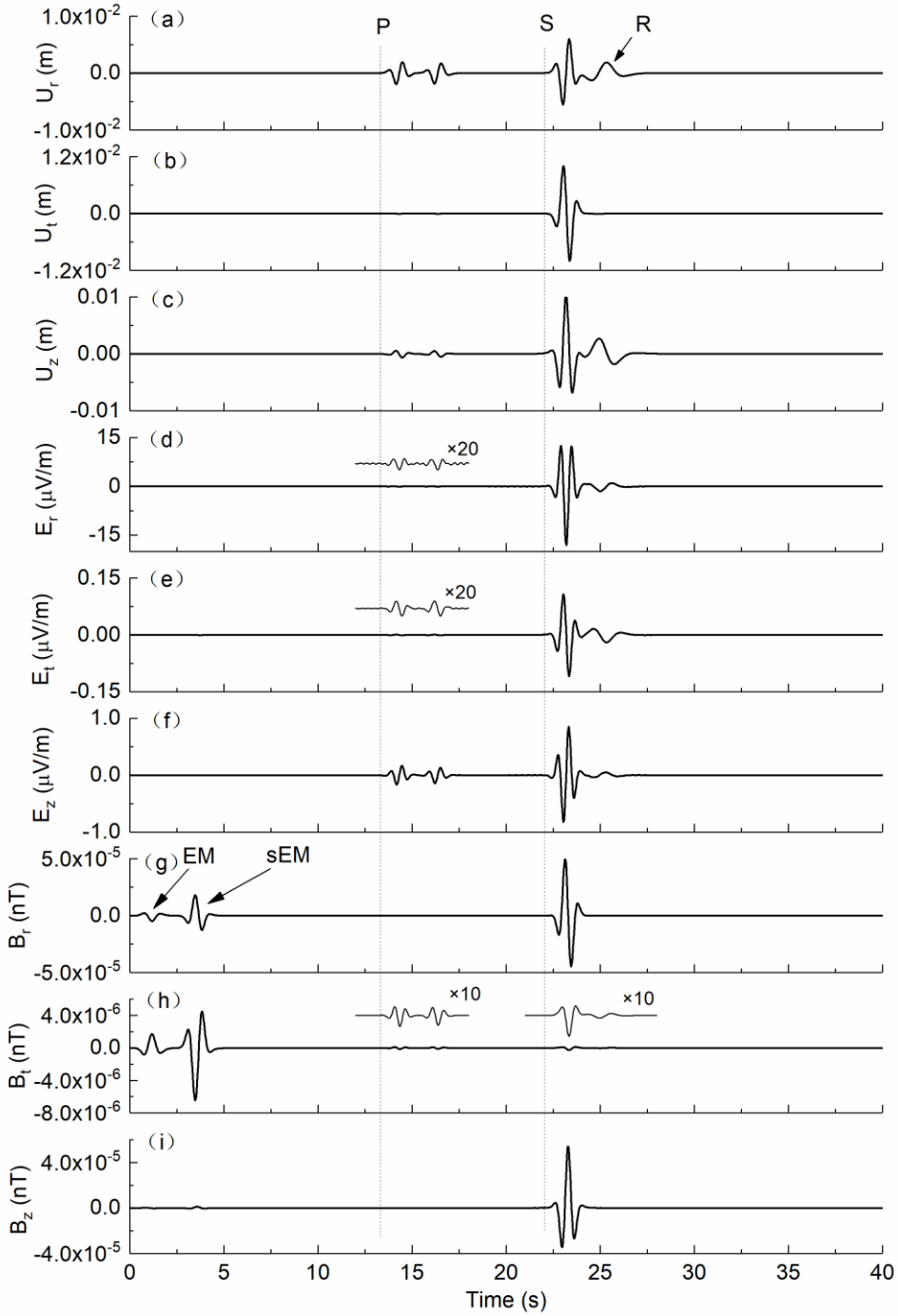

Figure 9. Seismic and EM responses generated by a fault slip in a half-space model. (a) - (c) are radial, tangential and vertical components of the displacement field; (d) - (f) are radial, tangential and vertical components of the electric field; (g) - (i) are radial, tangential and vertical components of the magnetic field.

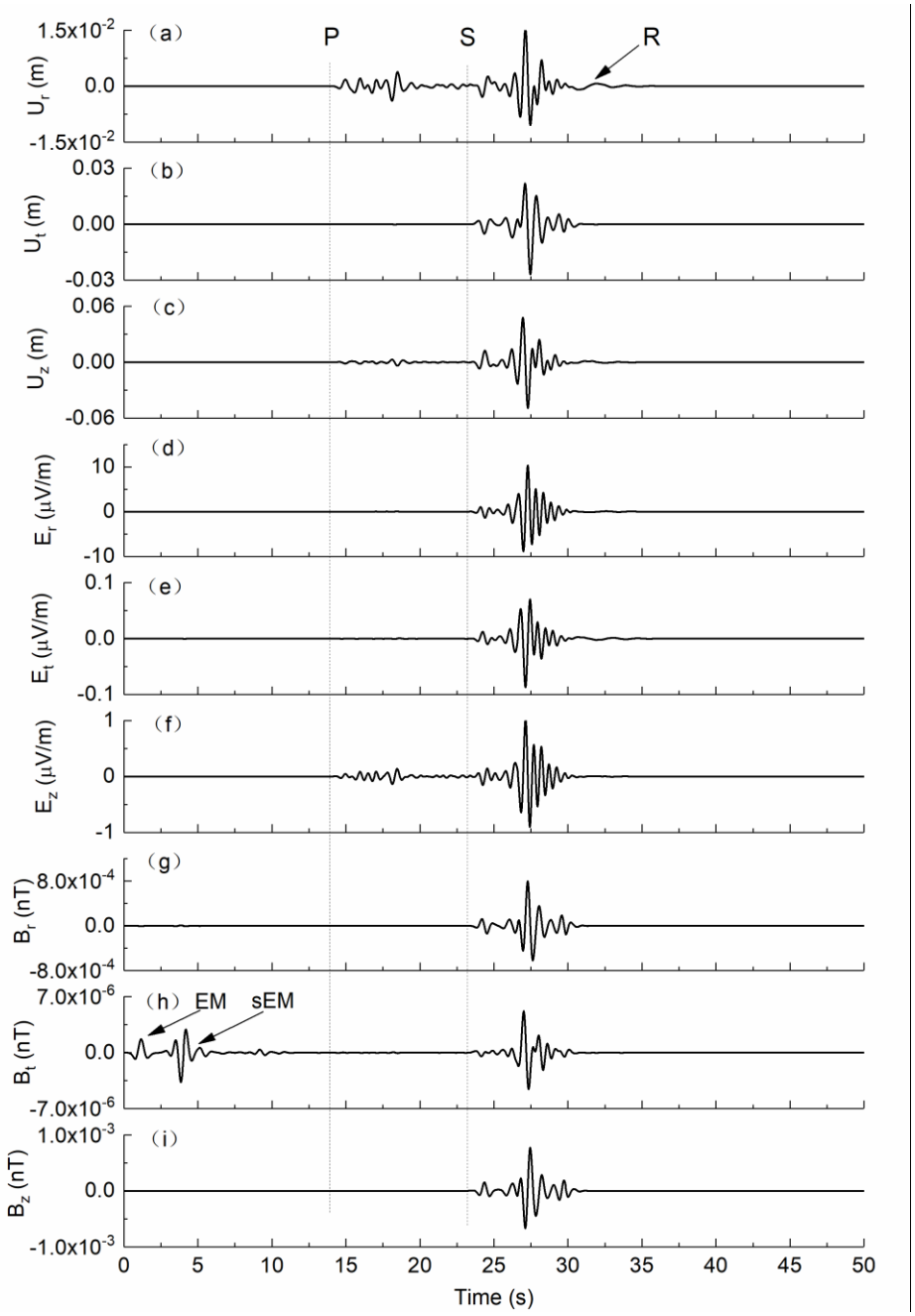

Figure 10. Seismic and EM responses generated by a fault slip source in a three-layers model. (a) - (c) are radial, tangential and vertical components of the displacement field; (d) - (f) are radial, tangential and vertical components of the electric field; (g) - (i) are radial, tangential and vertical components of the magnetic field.

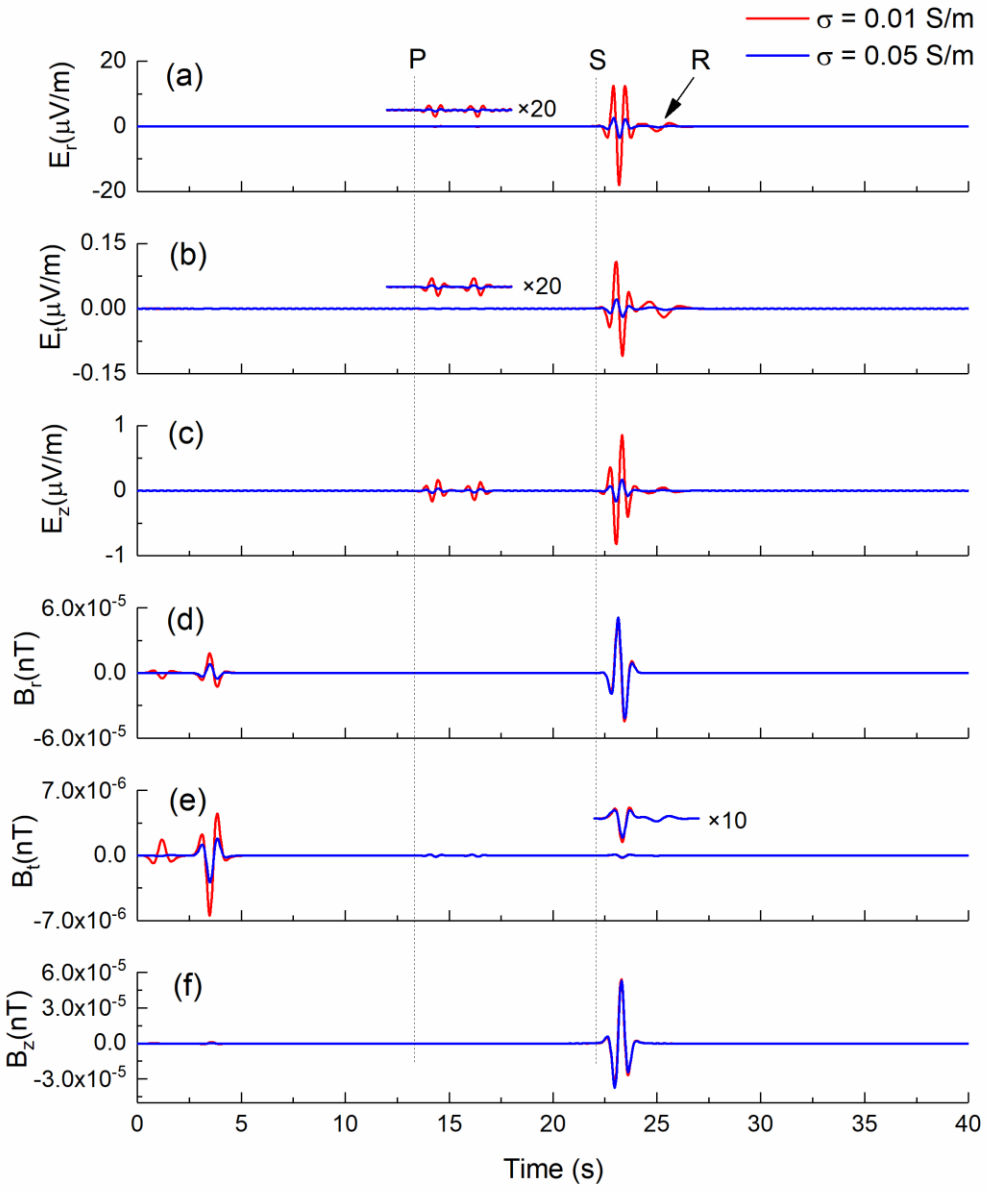

Figure 11. Seismic and EM responses calculated from different conductivities. The red lines denote the EM responses when the conductivity is 0.01 S/m, while the blue lines denote the EM responses when the conductivity is 0.05 S/m. (a) - (c) are three components of the electric field; (d) - (f) are three components of the magnetic field.

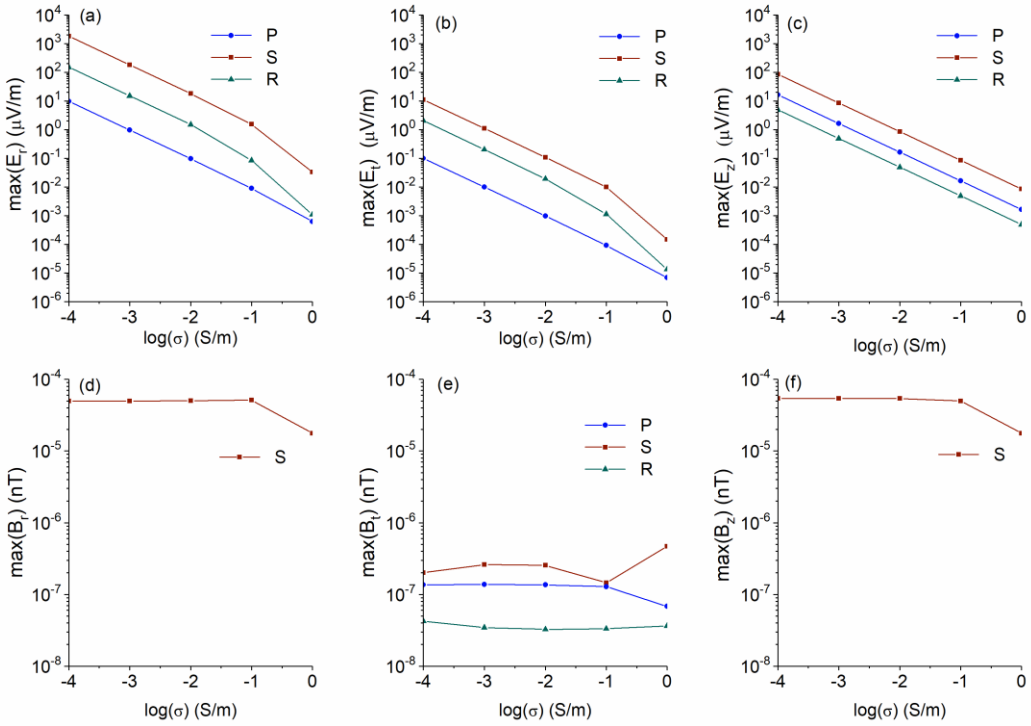

Figure 12. Variations of co-seismic electric and magnetic fields with the conductivity in a half-space model. (a) - (c) are three components of the electric field; (d) - (f) are three components of the magnetic field.

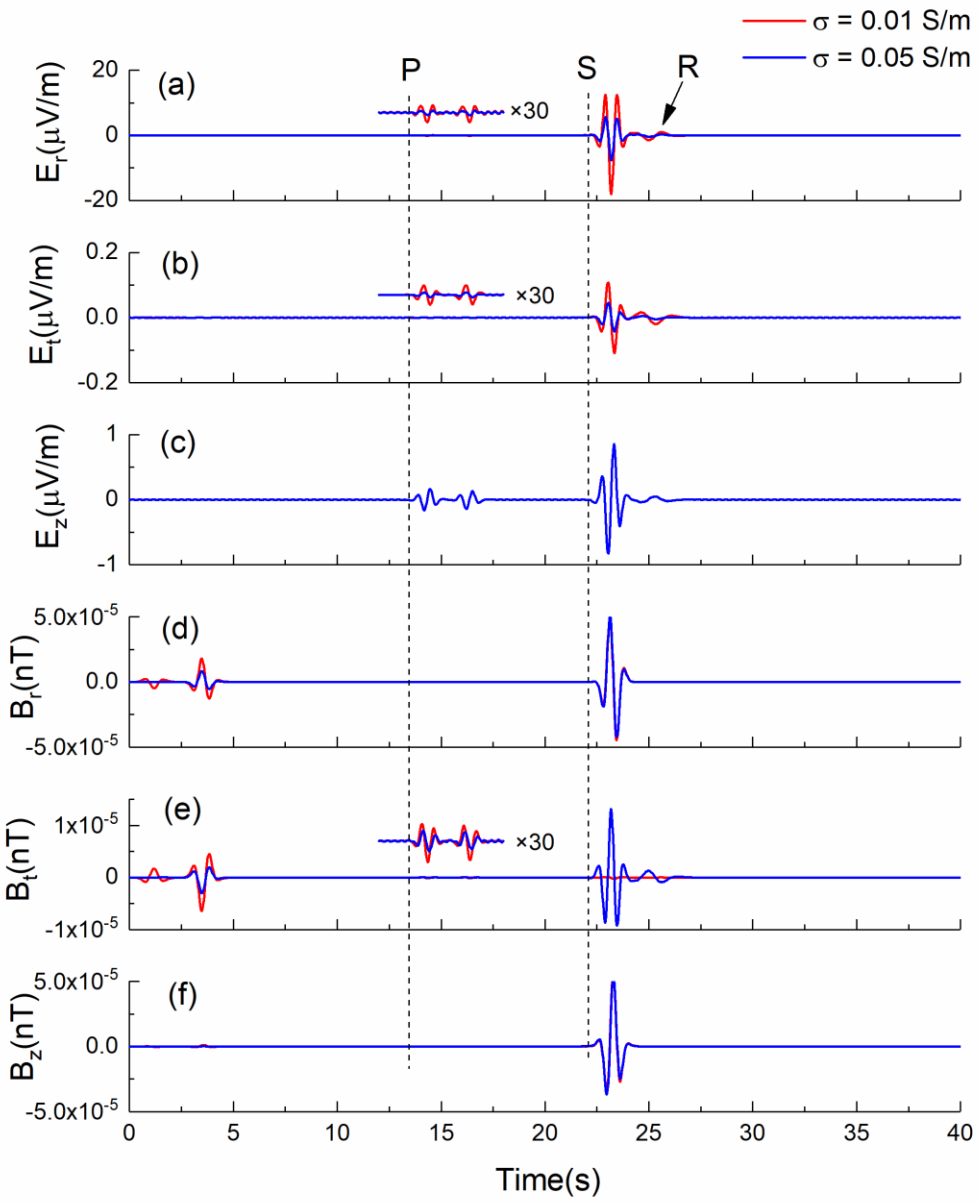

Figure 13. EM responses calculated by specifying the conductivity of the second layer in a two-layer model with 0.01 S/m (red) and 0.05 S/m (blue), respectively. (a) - (c) are three components of the electric field; (d) - (f) are three components of the magnetic field. The conductivity of the first layer is kept as 0.01 S/m.

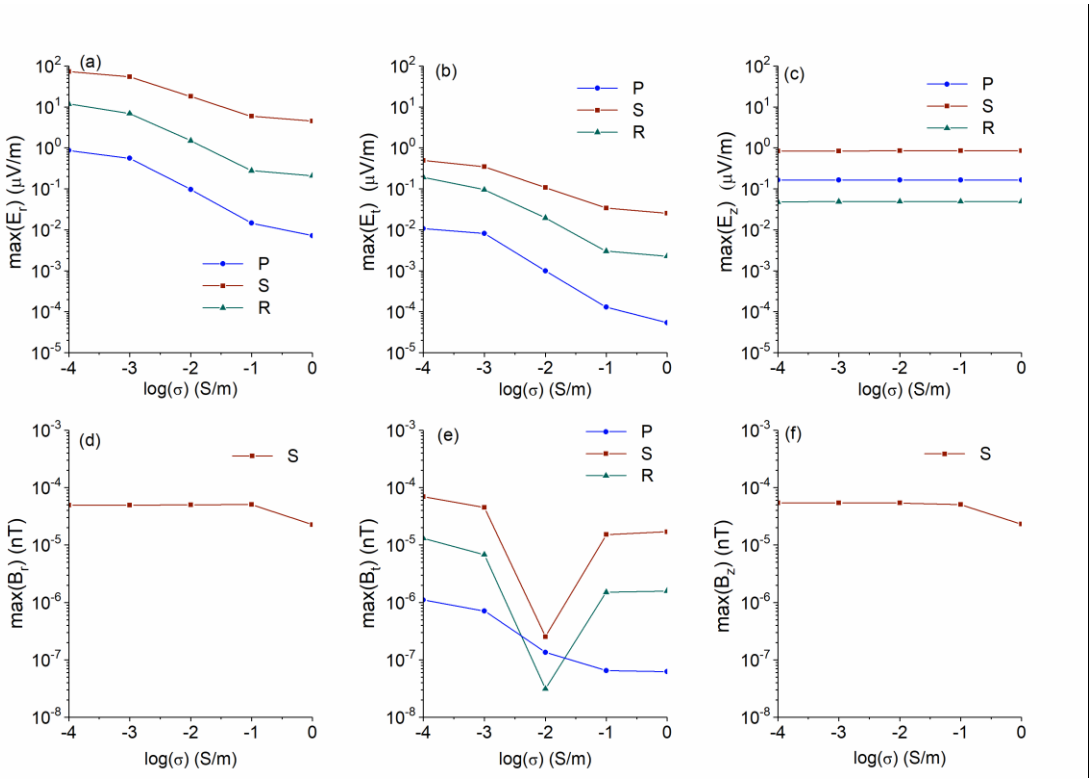

Figure 14. Variations of EM fields with the conductivity of the second layer (σ_2) changed in a two-layers model. (a) - (c) are three components of the electric field; (d) - (f) are three components of the magnetic field. The thickness of the first layer is 100 m, and the conductivity (σ_1) is 0.01 S/m. When $\sigma_2 = \sigma_1$, the two-layers model is equivalent to a half-space model.

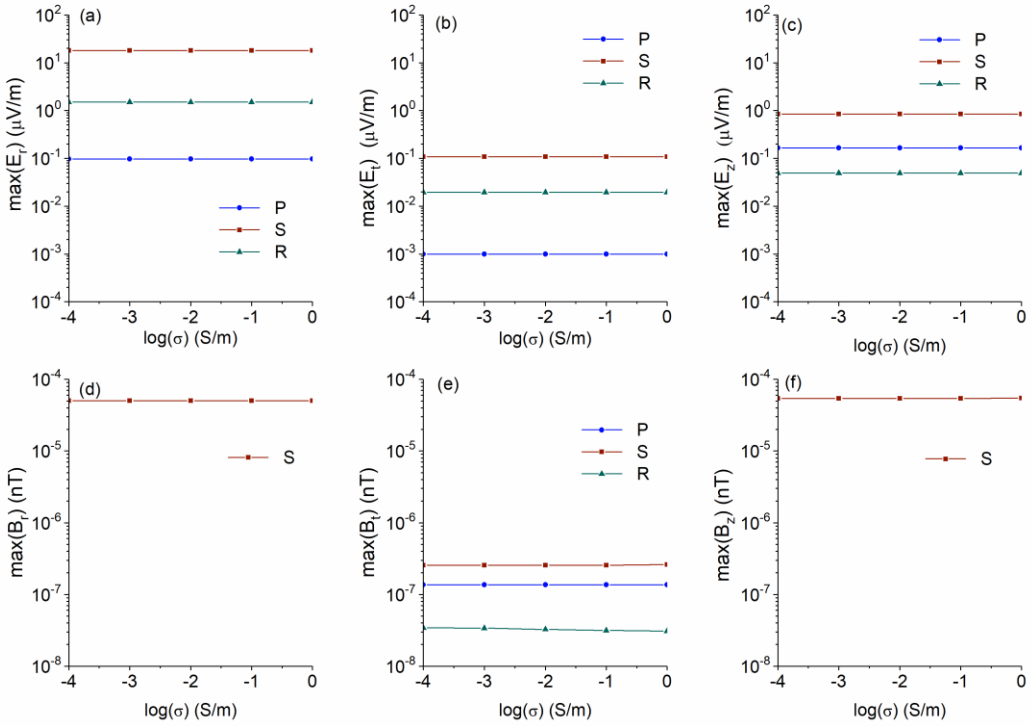

Figure 15. Same as Figure 14 but the thickness of the first layer is changed to 5000 m.